Received: 26 May 2019 | Revised: 12 December 2019 | Accepted: 26 January 2020

DOI: 10.1002/bit.27288

ARTICLE

BIOTECHNOLOGY AND BIOENGINEERING WILEY

A dynamic model linking cell growth to intracellular metabolism and extracellular by-product accumulation

João R. C. Ramos[1] | Alexander G. Rath[1,2] | Yvonne Genzel[1] | Volker Sandig[3] | Udo Reichl[1,4]

[1]Bioprocess Engineering, Max Planck Institute for Dynamics of Complex Technical Systems, Magdeburg, Germany

[2]Bioprocess Engineering, AMINO GmbH, Frellstedt, Germany

[3]Bioprocess Engineering, ProBioGen AG, Berlin, Germany

[4]Bioprocess Engineering, Otto von Guericke University Magdeburg, Chair of Bioprocess Engineering, Magdeburg, Germany

Correspondence
João R. C. Ramos, Bioprocess Engineering, Max Planck Institute for Dynamics of Complex Technical Systems, Bioprocess Engineering, Sandtorstr 1, 39106 Magdeburg, Germany.
Email: rodrigues_correira_r@mpi-magdeburg.mpg.de

Abstract

Mathematical modeling of animal cell growth and metabolism is essential for the understanding and improvement of the production of biopharmaceuticals. Models can explain the dynamic behavior of cell growth and product formation, support the identification of the most relevant parameters for process design, and significantly reduce the number of experiments to be performed for process optimization. Few dynamic models have been established that describe both extracellular and intracellular dynamics of growth and metabolism of animal cells. In this study, a model was developed, which comprises a set of 33 ordinary differential equations to describe batch cultivations of suspension AGE1.H-N.AAT cells considered for the production of α1-antitrypsin. This model combines a segregated cell growth model with a structured model of intracellular metabolism. Overall, it considers the viable cell concentration, mean cell diameter, viable cell volume, concentration of extracellular substrates, and intracellular concentrations of key metabolites from the central carbon metabolism. Furthermore, the release of metabolic by-products such as lactate and ammonium was estimated directly from the intracellular reactions. Based on the same set of parameters, this model simulates well the dynamics of four independent batch cultivations. Analysis of the simulated intracellular rates revealed at least two distinct cellular physiological states. The first physiological state was characterized by a high glycolytic rate and high lactate production. Whereas the second state was characterized by efficient adenosine triphosphate production, a low glycolytic rate, and reactions of the TCA cycle running in the reverse direction from α-ketoglutarate to citrate. Finally, we show possible applications of the model for cell line engineering and media optimization with two case studies.

KEYWORDS

animal cell, dynamic model, glycolysis, kinetic, metabolism, TCA cycle

1 | INTRODUCTION

Batch cultivation is one of the most commonly used operation modes for animal cell culture–based production of high-value biopharmaceuticals, that is, recombinant proteins and vaccines. The manufacturing of biopharmaceuticals requires a cell line with specific characteristics, which is generated through careful clone development and selection. Typically, in biopharmaceutical production, the price per dose of the final product is very high and careful process optimization and design is required to keep production costs low. In addition, it is necessary to guarantee product quality, safety, and efficacy to conform to the guidelines of regulatory authorities. For process optimization, detailed knowledge about the impact of parameters such as pH value, dissolved oxygen, and carbon dioxide concentration as well as medium composition on cell growth and product formation is often required. The optimization of these parameters is crucial for each cell line as specific characteristics can be scale dependent and vary for every cell line (Li, Vijayasankaran, Shen, Kiss, & Amanullah, 2010). In the past, the optimization of biological processes often relied on trial and error using a high number of experiments. With the additional use of mathematical methods, however, process design and optimization can be significantly accelerated (Mandenius & Brundin, 2008; Vicente, Mota, Peixoto, Alves, & Carrondo, 2011). In particular, decision-making based on models is a more rational approach regarding critical factors and responses of the process under investigation. One option is the use of design of experiments (DoE) approaches, where experiments are planned in a statistically optimal way to reduce the number of cultivations to be performed and to investigate the impact of parameters on product yield and product quality (Brendel & Marquardt, 2008; Kreutz & Timmer, 2009; von Stosch & Willis, 2017). A drawback of these methods, however, is their inability to handle more complex systems dynamics, for example, changes in critical cell properties or medium composition with process time, the release of inhibitory compounds into the cultivation broth, or the decrease in specific precursor concentrations required for product synthesis. Furthermore, conventional DoE approaches cannot explicitly consider the intracellular dynamics of animal cells, that is, crucial aspects of the central energy and carbohydrate metabolism.

Another option for process optimization and design is the well-known constraint-based modeling. This approach relies mainly on the estimation of flux distributions of metabolic networks using a pseudo-steady-state assumption (Kyriakopoulos et al., 2018; Stephanopoulos & Sinskey, 1993; Stephanopoulos & Stafford, 2002). As this approach deals with intracellular dynamics, it can support the establishment of DoE approaches. Examples are metabolic flux analysis (MFA) and flux balance analysis, which solve a linear system of equations to estimate the flux distribution in large-scale network models without taking into account any kinetic information (Hwang, Stephanopoulos, & Chan, 2004; Lee, Gianchandani, & Papin, 2006; Orth, Thiele, & Palsson, 2010; Stephanopoulos, 1999). For animal cells, various MFA models have been derived that rely on steady-state or pseudo-steady-state assumptions (Gombert & Nielsen, 2000). With these types of models, the response of a metabolic network can be used to assess possible steps toward achieving a significant increase in product yields. Furthermore, such models allowed a detailed characterization of several biotechnological processes and the unraveling of cell line-specific properties (Galleguillos et al., 2017; Gombert & Nielsen, 2000; Lee, Park, & Kim, 2011). Despite their widespread usage and simplicity, these models have limited applicability (due to their pseudo-steady-state assumption) and usually include no information about the reactions kinetics involved (Müller & Bockmayr, 2012).

For more realistic scenarios, dynamic models should be used to allow for the handling of complex and high-dimensional experimental data. Typically, this is achieved with the simulation of changes (such as metabolite concentration) over the time course using a set of ordinary differential equations (ODEs) with defined initial conditions and simplified, but biologically valid assumptions regarding cell growth, product formation, and enzyme kinetics (Bailey, 1998; Batt & Kompala, 1989). In particular, the formulated model should support a detailed analysis of interactions between different parts of the metabolic network (Sidoli, Mantalaris, & Asprey, 2004). Based on this, the understanding of the complex behavior of animal cells regarding growth and product formation can be increased. Linking such models with a more detailed description of protein glycosylation taking place in the endoplasmic reticulum and the Golgi apparatus, might even allow to uncover correlations of cultivation conditions with critical product quality attributes (i.e., antennary composition, sialylation, or core fucosylation) (Aghamohseni et al., 2014; Blondeel & Aucoin, 2018; Jimenez del Val, Nagy, & Kontoravdi, 2011). Eventually, options for increasing cell concentrations and product yields can be evaluated (Sidoli et al., 2004), and thus supporting processes intensification.

Despite these benefits, few dynamic models have been established that describe both cell growth and intracellular metabolism of animal cells. In contrast, various complex models have been implemented for *Escherichia coli* and yeasts that are validated and frequently used in metabolic redesign (Chassagnole, Noisommit-Rizzi, Schmid, Mauch, & Reuss, 2002; Khodayari, Zomorrodi, Liao, & Maranas, 2014; Rizzi, Baltes, Theobald, & Reuss, 1997). A widespread practice is the development of a dynamic model for cell growth and a constraint-based model for intracellular metabolism. For instance, for the human suspension cell line AGE1.HN, a simple model for cell growth (Rath et al., 2014) and a constraint-based model to describe intracellular metabolism (Niklas, Priesnitz, Rose, Sandig, & Heinzle, 2012; Priesnitz, Niklas, Rose, Sandig, & Heinzle, 2012) was established. So far, most models also focus only on a small part of intracellular pathways, that is, glycolysis (König, Bulik, & Holzhütter, 2012; Noguchi et al., 2013) and TCA (Bazil, Buzzard, & Rundell, 2010; Nazaret, Heiske, Thurley, & Mazat, 2009). These limitations can be attributed to the complexity of eukaryotic cells, scarcity of experimental data, and computational limitations. A particular challenge is the complexity of the metabolism of animal cells, which arises from the multitude of regulatory mechanism as

well as the high number of substrates taken up and by-products released. The lack of experimental data can be pinpointed to the laborious process of data collection and the lack of uniform quantification methods established to measure intracellular metabolite concentrations and enzyme activities; quenching of metabolism and sampling are also challenging. Finally, the establishment of dynamic models can be hampered by the availability of computational resources and limitations of algorithms required to estimate the large number of often poorly defined parameters.

In this study, a dynamic mathematical model was established for the human designer cell line AGE1.HN (provided by ProBioGen AG, Germany) that combines a segregated cell growth model with a structured model of intracellular metabolism. It was based on a model proposed by Rehberg et al. for adherent Madin–Darby canine kidney (MDCK) cells (Rehberg et al., 2013a,b; Rehberg et al., 2014a,b), where significant changes were required to describe cell growth of a suspension cell. Furthermore, in this case, the cell-death phase is considered, which is often neglected in cell growth models. More importantly, several aspects of the intracellular metabolic network were considered in more detail, such as the reactions that connect glycolysis and TCA and vice versa, and intracellular rates were used to simulate the accumulation of metabolic by-product in the extracellular environment. The model comprises a set of 33 ODEs accounting for cell growth (concentration of viable cells, mean cell diameter, volume of viable cells), and the concentration of key substrates and metabolites both at the intracellular and extracellular level. To describe the formation of the product α1-antitrypsin, a simple mass action law kinetic is used. Model validity was assessed using experimental data of four independent batch cultivations performed at 0.5 and 2.5 L scale in a chemically defined medium (42-MAX-UB) (Rath et al., 2014). Using the same set of parameters and specific initial conditions for each experiment, the model simulations capture well the overall dynamics of all experiments. Few exceptions include the dynamics of the intracellular concentrations of ribose-5-phosphate and succinate. The model is used to predict the impact of changes in media composition and maximum enzyme activity on the intracellular metabolism. Finally, the model addresses options for improving cell growth and measures toward the establishment of a more efficient metabolism.

2 | MATERIALS AND METHODS

2.1 | Cell line

The suspension cell line AGE1.HN was developed and patented by ProBioGen AG. It was derived from primary cells of human brain tissue and immortalized using adenoviral E1 A and B genes of human adenovirus type 5. Cells were then further modified to express the structural protein act 9 (pIX) of the same virus, which is known to be involved in the stabilization of the viral capsid and also in the control of apoptosis (Blanchard et al., 2011; Parks, 2005). The AGE1.HN.AAT cell line is a clone from AGE1.HN cells, which constitutively produces product α1-antitrypsin (Blanchard et al., 2011).

2.2 | Batch cultivation

Precultures were grown at 37°C in either 50 ml or 150 ml medium supplemented with 5 mM glutamine in 125 ml and 250 ml baffled shaker flasks, respectively.

The 0.5 and 2.5 L batch experiments were performed in stirred tank bioreactors (CellFerm-pro®; DasGip AG, Germany) using a chemically defined medium (42-MAX-UB; Teutocell AG, Germany) with initial cell concentration ranging from 5.5 to 7.5×10^5 cells/ml. The medium was supplemented with 30 mM glucose and 5 mM glutamine. Process parameters were controlled at pH 7.15, 40% pO_2, and 37°C, respectively. The experimental procedure and protocols used for the cultivations used here have been described in detail elsewhere (Borchers et al., 2013; Rath, 2017; Rath et al., 2014).

2.3 | Analytics

All samples were taken in triplicates and cell viability was determined with trypan blue. A Vi-Cell analyzer (TM XR; Beckman Coulter, Germany) was used to determine viable cell counts and cell diameters. The latter was determined by taking up to 100 stationary pictures of the cell broth sample. The overall mean cell diameter was estimated by averaging the mean cell diameter obtained from 100 images per sample. The total cell volume was obtained with the product of the mean cell volume and viable cell concentration.

For most of the extracellular metabolites, the quantification was done with a Bio-profile 100 Plus (Nova Biomedical). An exception was the quantification of pyruvate, which was performed by anion exchange chromatography (BioLC Dx-320 and DX-600; Thermo Scientific, Germany) as described by Genzel et al. (2005). Intracellular metabolites were measured using liquid chromatography–mass spectrometry according to Ritter, Wahl, Freund, Genzel, and Reichl (2010). Maximum enzyme activities were measured based on a protocol established by Janke (2012) for adherent MDCK cells that was modified for sampling of suspension cells. α1-Antitrypsin concentration in the supernatant of cell culture was determined with a sandwich enzyme-linked immunosorbent assay using a 95 well plate, established by Rath (2017). Additional information regarding experimental data is provided in Supporting Information Material S1 and the experimental procedure and protocols used for the cultivations used here have been described in detail elsewhere (Borchers et al., 2013; Rath, 2017; Rath et al., 2014).

2.4 | Model definition

The dynamic model developed describes both cell growth and metabolism by coupling a segregated growth model, which describes

cell growth dynamics in batch culture, with a structured model of the central carbon metabolism, which describes intracellular metabolite dynamics and connects extracellular product accumulation to the intracellular metabolic network. The segregated cell growth model is based on a model proposed for adherent MDCK cells (Rehberg et al., 2013a), which considers different cell size classes. This enables the estimation of the mean cell diameter and consequently the cell volume. Modeling cell volume was essential for the coupling of the cell growth model with the structured model of the intracellular metabolism considering that volumetric maximum enzyme activities depend on the cell-specific volume (Equation 42 in Supporting Information Material S2, enzyme concentration affected by changes in cell-specific volume). Further aspects regarding this modeling approach, including a discussion concerning the number of cell classes required in the segregated model, can be found elsewhere (Rehberg et al., 2013a,b; Rehberg et al., 2014b). Regarding the number of cell classes, five cell classes with linearly increasing diameter were chosen as to describe the experimental data collected for AGE1.HN.AAT cells. This was found as the minimum number of cell class required to describe the experimental data (data not shown) and it is in accordance with the number previously reported for MDCK cells (Rehberg et al., 2013a). In contrast, however, various modifications of the model developed for adherently growing cells were required to describe growth and metabolism of AGE1.HN.AAT suspension cells. The most important change concerned the lack of a surface area limitation, which is only relevant for growth of contact-inhibited adherent cells. In addition, due to the rather long cultivation time, cell death was taken into account to handle the loss of cell viability typically observed after substrate depletion. Although cell death phase is typically not relevant in industrial settings, this allowed detailed analyses of the switch from exponential cell growth to cell death and its implication on the cell metabolism. For the structured central carbon metabolism model, most assumptions regarding the set of active reactions were made according to previous studies of metabolism of this cell line (Niklas et al., 2011b; Priesnitz et al., 2012; Rath et al., 2014). An overview of the structure of the metabolic network is shown in Figure 1. The list of symbols used can be found in Supporting Information Material S5 and the model is provided in Supporting Information Material S6. Following in structure and basic assumptions the work for MDCK cells (Rehberg et al., 2013a,b; Rehberg et al., 2014a,b) and others (Mulukutla, Yongky,

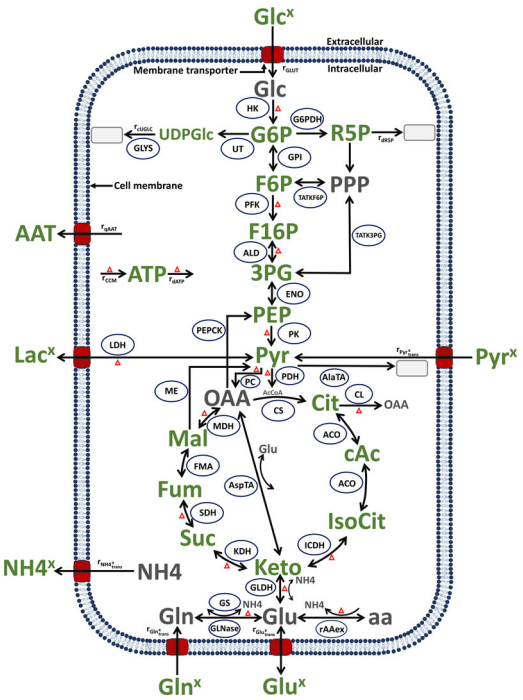

FIGURE 1 Simplified model of the central carbon metabolism of AGE.HN.AAT cells. In green: metabolites and product measured by Rath et al. (2014); in gray: metabolites not measured. Ellipsoids: enzymes considered in the model. Arrows: reactions or transport, with the arrowhead indicating the reaction or transport direction (for simplification, reversible reactions have an arrow for both directions). Gray rectangles: sinks or metabolites not accounted for in the model. Red triangles: all the reactions included in the energy balance. Abbreviations of metabolites and the product: 3PG, 3-Phosphoglycerate; AAT, α1-antitrypsin; AcCoA, acetyl coenzyme A; ATP, adenosine triphosphate; cAc, cis-Aconitate; Cit, citrate; F16P, fructose 1,6-biphosphate; F6P, fructose-6-phosphate; Fum, fumarate; G6P, glucose-6-phosphate; Glc, glucose (intracellular); Glc^x, glucose (extracellular); Gln, glutamine (intracellular); Gln^x, glutamine (extracellular); Glu, glutamate (intracellular); Glu^x, glutamate (extracellular); IsoCit, isocitrate; Keto, α-ketoglutarate; Lac^x, lactate (extracellular); Mal, malate; NH4, ammonium (intracellular); $NH4^x$, ammonium (extracellular); OAA, oxaloacetate; PEP, phosphoenolpyruvate; Pyr, pyruvate (intracellular); Pyr^x, pyruvate (extracellular); R5P, ribose-5-phosphate; SUC, succinate; UDPGlc, uridine diphosphate glucose. Abbreviations of enzymes and transport rates: HK, hexokinase; G6PDH, glucose-6-phosphate dehydrogenase; r_{dR5P}, reaction rate accounting for ribose-5-phosphate consumption; UT, Uridyl transferase; GLYS, glycogen synthetase; r_{uGLC}, reaction rate accounting for other uridine diphosphate glucose consumption; GPI, glucose-6-phosphate isomerase; TATKF6P, transaldolase and transketolase; TATK3PG, transaldolase and transketolase; PFK, phosphofructokinase; ALD, aldolase; r_{qAAT}, reaction rate accounting for product formation; ENO, rnolase; r_{CCM}, reaction rate accounting for overall ATP production; r_{dATP}, reaction rate accounting for overall ATP consumption; PK, pyruvate kinase; PEPCK, phosphoenolpyruvate-kinase; LDH, lactate dehydrogenase; PC, pyruvate carboxylase; PDH, pyruvate dehydrogenase; AlaTA, alanine transaminase; ME, malic enzyme; CS, citrate synthetase; CL, citrate lyase; ACO, aconitase; ICDH, isocitrate dehydrogenase; KDH, ketoglutarate dehydrogenase; AspTA, aspartate transaminase; SDH, succinate dehydrogenase; FMA, fumarase; MDH, malate dehydrogenase; GLDH, glutamate dehydrogenase; GS, glutamine synthetase; GLNase, glutaminase; r_{AAex}, amino acids degradation; r_{GLUT}, reaction rate accounting for extracellular glucose consumption; $r_{Pyr^x_{trans}}$, reaction rate accounting for extracellular pyruvate consumption; $r_{NH4^x_{trans}}$, reaction rate accounting for ammonium production from intracellular rates; $r_{Gln^x_{trans}}$, reaction rate accounting for extracellular glutamine consumption; $r_{Glu^x_{trans}}$, reaction rate accounting for extracellular glutamate consumption and/or production from intracellular rates [Color figure can be viewed at wileyonlinelibrary.com]

Grimm, Daoutidis, & Hu, 2015), reaction kinetics used were either simple or modified versions of first order kinetics, that is, Michaelis–Menten or Hill kinetics. In addition, the model explicitly takes into account maximum enzyme activities measured experimentally (Rath et al., 2014) and the degradation of amino acids (r_{AAex}) was estimated as proposed for MDCK cells (Rehberg et al., 2013b). In extension of the model proposed for MDCK cells (Rehberg et al., 2013b; Rehberg et al., 2014b), reactions that link the glycolytic pathway to the TCA cycle and vice versa were considered. Furthermore, various aspects of the intracellular metabolic network were considered in more detail. For instance, the ATP dynamic takes into account all reactions in which it is either directly consumed or produced, as well as other sources such as redox cofactors nicotinamide dinucleotide (NADH) and flavin-adenine-dinucleotide ($FADH_2$) (Xie & Wang, 1996). Furthermore, in contrast to the previous models, consumption rates of all extracellular substrates (glucose, glutamine, glutamate, lactate) were used as inputs for the intracellular metabolic network. The accumulation of extracellular by-products (lactate, ammonium, and glutamate) was estimated directly from intracellular metabolic rates. Another aspect of metabolism considered is the transamination of oxaloacetate (OAA) to ketoglutarate. The latter was added since previous studies of AGE1.HN cells suggested that this pathway strongly influences ammonium release and OAA synthesis (Priesnitz et al., 2012). Finally, due to lack of data regarding the distribution of intracellular metabolites in the cytoplasm and the mitochondria, it is assumed that all intracellular metabolites are homogeneously distributed.

In this modeling approach, the segregated cell growth model describes the macroscopic scale (dynamics of cells, product formation, and extracellular metabolites) while the structured model describes the intracellular metabolism including glycolysis, TCA, transamination, and energy metabolism on the microscopic scale. Accordingly, the macroscopic scale needs to be linked with the intracellular scale and vice versa (Equation 1) using r_{macro} (mmol·min^{-1}·L^{-1} for the volume referring to the bioreactor) and the corresponding intracellular rates r_i (mmol·min^{-1}·L^{-1} for the volume referring to the cells)

$$r_{macro} = r_i \frac{V_s^c X_v}{V_w}. \tag{1}$$

With cell-specific cell volume (V_s^c, L/cell; Equation 11), the viable cell concentration (X_v, cells/ml; Equation 6) and the conversion factor to the reference working volume of 1 ml (V_w, 10^{-3}) to convert viable cell volume per ml to viable cell volume per L. In the following, the ODEs for the segregated cell growth model and the structured model for the central carbon metabolism of AGE1.HN.AAT cells are introduced.

2.5 | Segregated cell growth model

The segregated cell growth model describes the dynamics of viable cells, substrates, product formation, and metabolic by-products on the macroscopic scale. It is assumed that cells transition from a first class (X_1, cells with the smallest diameter) to the last class (X_5, cells with the largest diameter) before dividing into two daughter cells (Equation 2–4).

$$\frac{dX_1}{dt} = r_{trans}(2X_5 - X_1 f) - k_d X_1, \tag{2}$$

$$\frac{dX_2}{dt} = r_{trans}(X_1 f - X_2) - k_d X_2, \tag{3}$$

$$\frac{dX_i}{dt} = r_{trans}(X_{i-1} - X_i) - k_d X_i, \quad \text{for } i = 3, \ldots N^c. \tag{4}$$

As in Rehberg et al. (2013a), five cell classes were considered to describe changes in the mean cell diameter during the time course of cultivation. In these five cell classes ($N^c = 5$), the transition rate (r_{trans}, Equation 5) controls the rate of cell division, the inhibition factor (f, Equation 7) limits the amount of cells that undergo cell division, and a cell death rate (k_d, Equation 8) accounts for cell death which occurs during the cultivation and specifically after substrate depletion.

The specific transition rate (r_{trans}, Equation 5) is estimated based on a Michaelis–Menten kinetic (μ) using the extracellular glucose concentration Glc^x multiplied with a constant (δ).

$$r_{trans} = \mu\delta \quad \text{with} \begin{cases} \mu = \mu_{max} \dfrac{[Glc^x]}{k^m_{Glc^x} + [Glc^x]} \\ \delta = \dfrac{1}{2^{1/N^c} - 1} \end{cases} \tag{5}$$

This constant (δ) depends on the number of different cell classes considered in the model (for a mathematical explanation; Rehberg et al., 2013a). The parameters μ_{max}, Glc^x, and $k^m_{Glc^x}$ are the maximum specific cell growth rate, the extracellular glucose concentration, and the Michaelis–Menten constant, respectively.

The viable cell concentration (X_v) is given by the sum of cells in each class.

$$X_v = \sum_{i=1}^{N^c} X_i. \tag{6}$$

The inhibition factor (f) accounts for a growth inhibition of viable cells by taking into account the extracellular glucose concentration (Glc^x).

$$f = 1 - e^{-\alpha \frac{Glc^x}{X_v}}. \tag{7}$$

Note that this inhibition factor corresponds to the fraction of cells that start the division process (transition from the first class to the last cell class). Therefore, it has a maximum value of 1 (corresponding to 100% of the first cell class starting the division process) and a minimum of 0 (when 0% of the cells of the first cell class start the division process). To adjust the changes on the inhibition factor in all cultivations a scaling constant (α) is used. Note that the fraction of nondividing cells from the first cell class was not considered in the

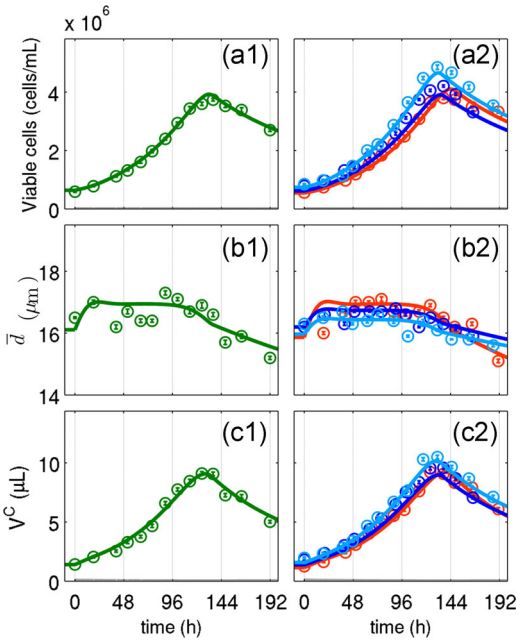

FIGURE 2 Suspension AGE1.HN.AAT cell growth in a chemically defined medium for four small-scale cultivations. Viable cell concentration (A1–2), mean cell diameter (B1–2), and viable cell volume (C1–2). Data and error bar represent mean and standard deviation of three technical triplicates for four independent experiments (0.5 L ○, ○ and 2.5 L ○, ○ stirred tank bioreactors); lines: model simulations. Experimental data used for parameter estimation (A1, B1, C1) [Color figure can be viewed at wileyonlinelibrary.com]

growth-related glucose consumption (Equation 12), but only in the maintenance related glucose consumption (Equation 13).

To account for the loss of cell viability, especially after substrate depletion (Figures 2 and 3), the specific cell death rate (k_d) considers a basal cell death rate ($k_d^{\min}$) during the exponential cell growth phase (caused by cell damage, age, etc.) plus an additional term which approaches $k_d^{\max}$. The increase of $k_d^{\max}$ is considered to be inversely correlated with the effective cell growth rate (), a correlation that has been used previously (Sanderson, Barford, & Barton, 1999; Zhou, Bi, Zeng, & Yuan, 2006).

$$k_d = k_d^{\min} + k_d^{\max}\left(\frac{\beta}{\beta + \mu f}\right)^2. \tag{8}$$

The parameter β is a constant manually adjusted to fit the overall increase in k_d with cultivation time. This implies that the cell death is not explicitly assumed to depend on the accumulation of by-products such as ammonium or lactate as described in various other cell growth models. Implicitly, however, inhibition is accounted for to a certain degree as by-products accumulate while substrates such as glucose, glutamine, and pyruvate are consumed and the substrate level (i.e., glucose concentration) directly influences the effective

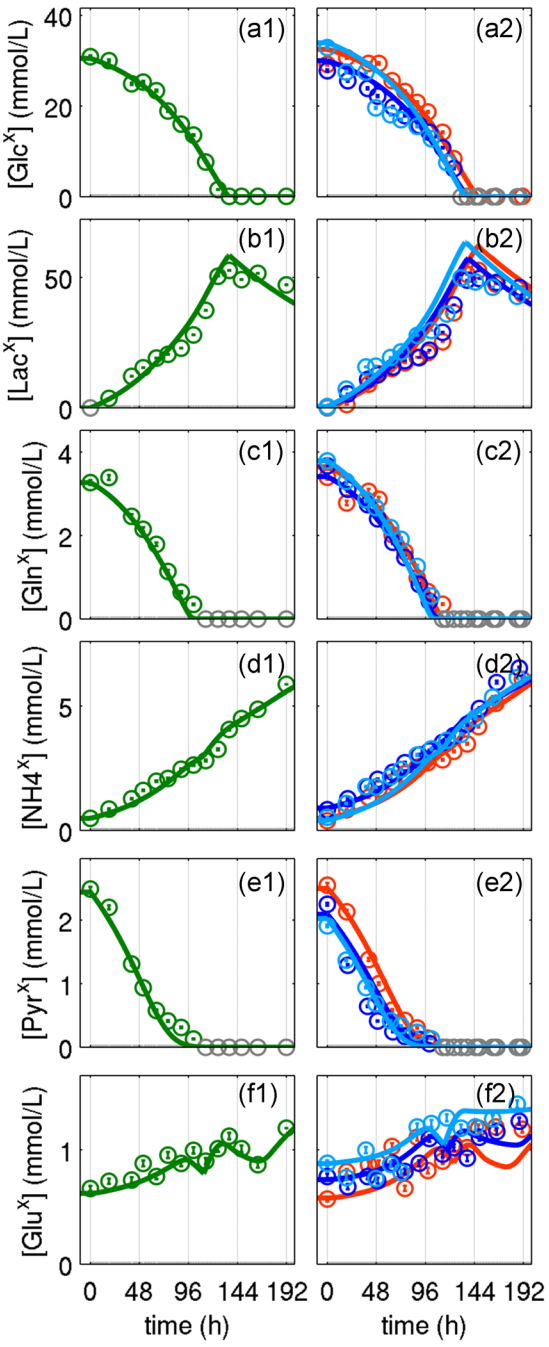

FIGURE 3 Extracellular substrates and metabolic by-products for suspension AGE1.HN.AAT cell growth in a chemically defined medium. Glucose (A1–2), lactate (B1–2), glutamine (C1–2), extracellular ammonium (D1–2), pyruvate (E1–2), and glutamate (F1–2). Data and error bar represent mean and standard deviation of three technical triplicates for four independent experiments (0.5 L ○, ○ and 2.5 L ○, ○ stirred tank bioreactors); lines: model simulations. Experimental data used for parameter estimation (A1, B1, C1, D1, F1). The gray lines indicate the limit of quantification for each metabolite and the gray data points are under the limit of quantification [Color figure can be viewed at wileyonlinelibrary.com]

growth rate. If required, the corresponding term for by-product accumulation could be easily added to the k_d kinetics.

Taking into account the total number of cells of each class (X_i), the mean cell diameter ($\bar{d}$) is determined by Equation (9).

$$\bar{d} = \sum_{i=1}^{N^c} \left(d_m + \frac{d_c - d_m}{N^c - 1}(i-1) \right) \frac{X_i}{X_v}. \tag{9}$$

With equidistant cell diameters ranging from a minimum value (d_m), where cell division is initiated (if not inhibited), to a critical value (d_c), where it divides in two daughter cells (i.e., the first cell class [X_1] has the lowest diameter [d_m] and the last cell class [X_5] has the largest diameter [d_c]). The estimated mean cell diameter in the model is fitted to the mean cell diameter calculated from the experimental data collect by Rath et al. (Borchers et al., 2013; Rath et al., 2014). Note that both d_c and d_m were manually adjusted for each experiment to minimize the difference between the experimental and simulated viable cell volume. Based on the mean diameter (d_c), it is possible to calculate the viable cell volume (V^c, μL) and the cell-specific cell volume (V_s^c, L/cell) using Equations (10) and (11), respectively.

$$V^c = \pi \frac{\bar{d}^3}{6} X_v 10^{-9}, \tag{10}$$

$$V_s^c = \frac{V^c}{X_v} 10^{-6}. \tag{11}$$

Cells consume substrates and release metabolic by-products over the time course of cultivations, that is, glucose, glutamine, and glutamate as well as lactate and ammonium. Regarding glucose consumption, growth (r_{x/Glc^x}) and maintenance (r_{m/Glc^x}) rates are considered as described in Rehberg et al. (2013a).

$$r_{x/Glc^x} = \mu \left(X_1 f + \sum_{i=2}^{N^c} X_i \right) Y_{x/Glc^x}, \tag{12}$$

where the cell growth-specific yield is Y_{x/Glc^x}. And for maintenance:

$$r_{m/Glc^x} = m_{Glc^x} V^c \Theta[Glc^x], \tag{13}$$

where m_{Glc^x} is a constant and Θ is a step function, which is one for $Glc^x > 0$ and zero otherwise.

This yields the following ODE that describes the dynamics of extracellular glucose uptake.

$$\frac{d[Glc^x]}{dt} = -r_{X/Glc^x} - \quad r_{m/Glc^x}. \tag{14}$$

In contrast to glucose, for other extracellular metabolites such as glutamine and pyruvate, a simpler approach to describe their consumption was used since cell growth was assumed to be independent of their presence in the medium. For this reason, the dynamics of the remaining extracellular substrates and the metabolic by-products were described with a Michaelis–Menten-like kinetic. This application is similar to the approach previously used for this cell line (Rath et al., 2014) and other authors (Barford, Phillips, & Harbour, 1992; de Tremblay, Perrier, Chavarie, & Archambault, 1992; Luni, Marth, & Doyle, 2012; Marín-Hernández et al., 2011; Uldry, Ibberson, Hosokawa, & Thorens, 2002). Furthermore, it is assumed that the intracellular concentration of certain amino acids, such as glutamate and glutamine, has an impact on their consumption rate as their intracellular concentration has been shown to impact transporter capacity (Hyde, Taylor, & Hundal, 2003). Note that, ammonium accumulation was simulated accounting for the spontaneous degradation of extracellular glutamine, as reported in Ozturk and Palsson (1990), and all other intracellular reactions where it is either consumed or produced. These reactions include two enzyme-catalyzed reactions (glutaminase, glutamine synthetase) and amino acid catabolism (r_{AAex}), which were lumped in one reaction ($r_{NH4^x_{trans}}$). Since the intracellular ammonium concentration could not be quantified, it is assumed that ammonium does not accumulate intracellularly. Finally, product formation is assumed to be growth-related and a mass action kinetic was used. Refer to Supporting Information Material for each kinetic (Equations in Supporting Information Material S2).

$$\frac{d[Gln^x]}{dt} = -r_{Gln^x_{trans}} - r_{dGln^x}, \tag{15}$$

$$\frac{d[Glu^x]}{dt} = -r_{Glu_{trans}} \frac{V_s^c X_v}{V_w}, \tag{16}$$

$$\frac{d[NH4^x]}{dt} = r_{dGln^x} + r_{NH4^x_{trans}}, \tag{17}$$

$$\frac{d[Lac^x]}{dt} = r_{LDH} \frac{V_s^c X_v}{V_w} - r_{Lac^x_{trans}}, \tag{18}$$

$$\frac{d[Pyr^x]}{dt} = -r_{Pyr^x_{Trans}}, \tag{19}$$

$$\frac{d[AAT]}{dt} = r_{qAAT.} \tag{20}$$

2.6 | Structured model of the central carbon metabolism

The structured model for central carbon metabolism includes reactions from glycolysis, citric acid cycle, glutaminolysis, transamination, and the pentose phosphate pathway. To cover changes in extracellular and intracellular metabolites concentrations, this model requires several growth-related variables such as mean cell volume and glucose uptake rate, so it was linked to the segregated cell growth model.

2.7 | Glycolysis

The following set of equations (Equations 21–29) was used to describe the dynamics of intracellular metabolites involved in the glycolytic pathway. In each ODE, changes in the intracellular metabolite concentrations were obtained considering consumption or production in different reactions or transport. Refer to Supporting Information Material S2 for individual reactions kinetics. Note that the term $\mu f[C]$ expresses the dilution of each intracellular metabolite (C) by changes in the cell volume caused by the effective growth rate (μf).

$$\frac{d[\mathrm{Glc}]}{dt} = r_{\mathrm{GLUT}} - r_{\mathrm{HK}} - \mu f\,[\mathrm{Glc}], \tag{21}$$

$$\frac{d[\mathrm{G6P}]}{dt} = r_{\mathrm{HK}} - r_{\mathrm{GPI}} - r_{\mathrm{G6PDH}} - r_{\mathrm{UT}} - \mu f\,[\mathrm{G6P}], \tag{22}$$

$$\frac{d[\mathrm{F6P}]}{dt} = r_{\mathrm{GPI}} - r_{\mathrm{PFK}} + r_{\mathrm{TATKF6P}} - \mu f\,[\mathrm{F6P}], \tag{23}$$

$$\frac{d[\mathrm{R5P}]}{dt} = r_{\mathrm{G6PDH}} - r_{\mathrm{TATKF6P}} - r_{\mathrm{TATK3PG}} - r_{\mathrm{dR5P}} - \mu f\,[\mathrm{R5P}], \tag{24}$$

$$\frac{d[\mathrm{UDPGlc}]}{dt} = r_{\mathrm{UT}} - r_{\mathrm{cUGlc}} - r_{\mathrm{GLYS}} - \mu f\,[\mathrm{UDPGlc}], \tag{25}$$

$$\frac{d[\mathrm{F16P}]}{dt} = r_{\mathrm{PFK}} - r_{\mathrm{ALD}} - \mu f\,[\mathrm{F16P}], \tag{26}$$

$$\frac{d[\mathrm{3PG}]}{dt} = 2r_{\mathrm{ALD}} - r_{\mathrm{ENO}} + r_{\mathrm{TATK3PG}} - \mu f\,[\mathrm{3PG}], \tag{27}$$

$$\frac{d[\mathrm{PEP}]}{dt} = r_{\mathrm{ENO}} - r_{\mathrm{PK}} - r_{\mathrm{PEPCK}} - \mu f\,[\mathrm{PEP}], \tag{28}$$

$$\frac{d[\mathrm{Pyr}]}{dt} = r_{\mathrm{PK}} - r_{\mathrm{LDH}} - r_{\mathrm{PDH}} + r_{\mathrm{ME}} - r_{\mathrm{PC}} + r_{\mathrm{Pyr}^{x}_{\mathrm{trans}}} \frac{V_w}{(V_s^c X_v)} + r_{\mathrm{Lac}^{x}_{\mathrm{trans}}} \frac{V_w}{(V_s^c X_v)} - r_{\mathrm{AlaTA}} - \mu f\,[\mathrm{Pyr}]. \tag{29}$$

2.8 | Citric acid cycle, glutaminolysis, and transamination

Glycolysis was linked to the TCA cycle through different enzymes like pyruvate dehydrogenase (PDH), phosphoenolpyruvate carboxylase (PEPCK), pyruvate carboxylase (PC), and malic enzyme (ME). The following set of equations (Equations 30–40) introduces the ODEs used to describe the dynamics of the different metabolites of this pathway. For individual enzyme kinetics, refer to Supporting Information Material S2.

$$\frac{d[\mathrm{AcCoA}]}{dt} = r_{\mathrm{PDH}} - r_{\mathrm{CS}} - \mu f\,[\mathrm{AcCoA}], \tag{30}$$

$$\frac{d[\mathrm{Cit}]}{dt} = r_{\mathrm{CS}} - r_{\mathrm{ACO}} - r_{\mathrm{CL}} - \mu f\,[\mathrm{Cit}], \tag{31}$$

$$\frac{d[\mathrm{cAc}]}{dt} = r_{\mathrm{ACO}} - r_{\mathrm{ACO2}} - \mu f\,[\mathrm{cAc}], \tag{32}$$

$$\frac{d[\mathrm{Isocit}]}{dt} = r_{\mathrm{ACO2}} - r_{\mathrm{ICDH}} - \mu f\,[\mathrm{Isocit}], \tag{33}$$

$$\frac{d[\mathrm{Gln}]}{dt} = r_{\mathrm{Gln}^{x}_{\mathrm{trans}}} \frac{V_w}{(V_s^c X_v)} - r_{\mathrm{Glnase}} + r_{\mathrm{GS}} - \mu f\,[\mathrm{Gln}], \tag{34}$$

$$\frac{d[\mathrm{Glu}]}{dt} = r_{\mathrm{GLU}_{\mathrm{trans}}} + r_{\mathrm{Glnase}} + r_{\mathrm{AAex}} - r_{\mathrm{GS}} - r_{\mathrm{GLDH}} + r_{\mathrm{AspTA}} - \mu f\,[\mathrm{Glu}], \tag{35}$$

$$\frac{d[\mathrm{Keto}]}{dt} = r_{\mathrm{ICDH}} - r_{\mathrm{KDH}} + r_{\mathrm{GLDH}} - r_{\mathrm{AspTA}} - \mu f\,[\mathrm{Keto}], \tag{36}$$

$$\frac{d[\mathrm{Suc}]}{dt} = r_{\mathrm{KDH}} - r_{\mathrm{SDH}} - \mu f\,[\mathrm{Suc}], \tag{37}$$

$$\frac{d[\mathrm{Fum}]}{dt} = r_{\mathrm{SDH}} - r_{\mathrm{FMA}} - \mu f\,[\mathrm{Fum}], \tag{38}$$

$$\frac{d[\mathrm{Mal}]}{dt} = r_{\mathrm{FMA}} - r_{\mathrm{MDH}} - r_{\mathrm{ME}} - \mu f\,[\mathrm{Mal}], \tag{39}$$

$$\frac{d[\mathrm{OAA}]}{dt} = r_{\mathrm{MDH}} + r_{\mathrm{AspTA}} + r_{\mathrm{CL}} + r_{\mathrm{PC}} - r_{\mathrm{PEPCK}} - r_{\mathrm{CS}} - \mu f\,[\mathrm{OAA}]. \tag{40}$$

2.9 | Energy metabolism

ATP is either generated directly in some reactions or produced from several precursors such as NADH and $FADH_2$ through oxidative phosphorylation (Equation 41). On the other hand, ATP is consumed for cell growth, maintenance metabolism, various other reactions of glycolysis and the TCA cycle, and in several futile cycles. Here, ATP production and its usage were lumped in the rates r_{CCM} and r_{dATP}, respectively. Furthermore, we assume that energy precursors are not accumulated but used directly in the oxidative phosphorylation (electron transport) pathway, and that 2.5 ATP are produced from NADH and 1.5 ATP from $FADH_2$ as reported in Salway (2004) and Xie and Wang (1996). For simplification and lack of experimental data for most of these cofactors, their regulation or their homeostasis-driven regulation are no taken into account, which evidently could limit model predictions. The following ODE (Equation 41) was used.

$$\frac{d[\mathrm{ATP}]}{dt} = r_{\mathrm{CCM}} - r_{\mathrm{dATP}} - \mu f\,[\mathrm{ATP}] \tag{41}$$

2.10 | Parameter fitting and model simulation

Parameter fitting and visualization of the results was carried out in MATLAB (version R2012b; Mathworks, Inc.). For handling of the model and the data, the Systems Biology Toolbox 2 developed by Schmidt and Jirstrand (2006) was used. Integration of ODEs was performed with CVODE from SUNDIALS (Cohen & Hindmarsh, 1996); the enhanced scatter search (eSS) algorithm was used for stochastic global optimization (Egea, Balsa-Canto, García, & Banga, 2009; Egea, Martí, & Banga, 2010).

In a first step, parameters from the segregated cell growth model (Equations 2–14) were fitted using one of the available experimental data sets. For optimization, the initial values of parameters were estimated from experimental data (i.e., the specific cell growth rate), or taken from literature (Rehberg et al., 2013b; Rehberg et al., 2014b). Next, variables from this model (growth-related glucose consumption rate, maintenance related glucose consumption rate, cell-specific volume, cell growth rate) were used as input for the structured central carbon metabolism model and the parameters of this model were fitted to the same data set as before. In this step, dynamics of some extracellular metabolites (extracellular glutamine, extracellular pyruvate, extracellular lactate, extracellular glutamate) were also considered since these were predicted directly from the intracellular ODEs. Overall, 132 parameters were fitted using about 353 data points. Due to model complexity, data variability, and the fact that only one data set was used for parameter estimation, overfitting cannot be excluded.

The established model was used with different initial conditions, and the same parameter set to simulate three other batch cultivations. Therefore, the initial conditions for the state variables of the

segregated cell growth model were adjusted manually within the error of the experimental data at the start of the cultivation. The initial conditions of the structured intracellular model states were obtained from the simulation of a preculture from the late exponential growth phase. To simulate the preculture growth until the exponential growth phase (about 75 hr), the known concentrations of all compounds in the medium was used as initial conditions. The initial values of the intracellular states were taken from the first sampling time point (in cases where no data was available, we used reasonably low initial concentrations from previous studies of our group and general literature). Next, the estimated basal cell death rate (k_d^{min}) was increased by a factor of 300 for 7 min cultivation time to take into account the drop in intracellular metabolite concentrations resulting from sampling, centrifugation, and resuspension of cells before measurements were performed. Note that sampling, centrifugation, and resuspension of cells lasted around 7 min in this case and thus it was assumed that the cells metabolic activity would persist.

3 | RESULTS AND DISCUSSION

3.1 | Model simulation of the cell growth dynamics

In the following, model simulations and experimental data for the concentration of viable cells, the mean cell diameter, and the total cell volume are shown (Figure 2) for four cultivations at 0.5–2.5 L scale performed by Rath et al. (Borchers et al., 2013; Rath et al., 2014). Model simulations are based on specific initial conditions of each cultivation but use the same set of parameters (Table 3 in Supporting Information Material S3). Note that the simulations also cover the time period after achieving the maximum cell concentration starting at about 130 hr after inoculation, which is often neglected in cell growth models, for instance in previous studies dealing with the same cell line (Borchers et al., 2013).

After inoculation with about 6.10^5 cells/ml, all cultivations started with exponential cell growth until maximum cell concentration ranging from 3.8 to 4.6×10^6 cells/ml at about 130 hr were achieved. Following a similar trend as cell concentration, the viable cell volume (V^c) increased from about 1.3 µl to a maximum in the range of 9 to 10.2 µl, before onset of cell lysis. Similar to findings of Rehberg et al. (2013a) for adherent MDCK cells, the variation between cultivations is low for V^c and, to a lesser degree, also for cell diameters. Initially, cell diameters ranged from 15.8 to 16.2 µm (Figure 2b). After about 18 hr, a mean cell diameter of 16.5–17.0 µm was achieved, which decreased after about 110 hr to a minimum of 15.1–15.8 µm. Although the experimental data is rather noisy, the same trend (higher mean cell diameter which decreases at later growth cell growth phase) is observed for all cultivations, as it is also typically observed for suspension cell line cultivations. The model simulations described well the changes in cell concentration and the variations in mean cell diameters over the cultivation period (Figure 2a,b). Based on the good estimation of the mean cell diameter, the viable cell volume was also fitted well (Figure 2c). Modeling the cell volume is essential because usually a delay between the increase in viable cell concentration compared to the viable cell volume during cell growth is observed (Nielsen, Reid, & Greenfield, 1997) and this delay was accounted for in other parts of the model. In particular, the model simulations cover changes of the mean cell diameter of about 10% during the cultivation of AGE1.HN.AAT cells. Modeling such minor changes in diameter is relevant since the consideration of this effect results in up to 30% variation of the mean cell-specific volume (V_s^c) (Equations 10–11 in Supporting Information Material S2, Figure S1b in Supporting Information Material S4). Furthermore, since the maximum enzyme activity is expressed per V_s^c (Equation 42), this would lead to up to 15% change in the volumetric maximum enzyme activities

$$K_e^{max} = \frac{v_e E_{level}}{V_s^c}, \tag{42}$$

where the volumetric maximum enzyme activity (K_e^{max}) is dependent on the cell-specific volumetric enzyme activity v_e, a constant measured experimentally, the enzyme level (E_{level}, constant), and the cell-specific volume (V_s^c). The enzyme level (E_{level}) is a term proposed for MDCK cells (Rehberg et al., 2014b) and corresponds to the experiment-specific relative enzyme level of the cell population, which indicates that total enzyme content changes for each experiment when compared with a standard value. As for intracellular metabolite concentrations, the volumetric maximum enzyme activity was not constant due to changes in the mean cell diameter over time (Figure 2b), which correlates with the cell-specific volume. In other words, a smaller cell-specific volume would lead to a higher volumetric maximum enzyme activity and vice versa. This correlated well with experimental observations for this cell line by Rath et al. (2014), where the overall volumetric enzyme activity of AGE1.HN cells was higher during the stationary growth phase compared to the exponential phase. Increased cell diameters were also found during the exponential growth phase of adherent MDCK cells (Rehberg et al., 2013a,b; Rehberg et al., 2014b). Similar changes in maximum enzyme activities could also be due to changes in transcriptomics and subsequent alterations in intracellular protein concentrations. Corresponding assays could, however, not be performed within the scope of this study.

Overall, the segregated growth model used in this study described well the growth of suspension AGE1.HN.AAT cells. Taking explicitly into account changes in the mean cell diameter enables the estimation of the time course of the cell-specific volume. This facilitates the establishment of structured intracellular models in case maximum enzyme activities are measured, as both changes in rates as well as changes in enzyme activities can be considered for model fitting.

3.2 | Model simulation of substrate and metabolic by-product dynamics

In the following, model simulations are presented alongside experimental data for extracellular substrates and metabolic by-products for the four cultivations at 0.5–2.5 L scale.

Extracellular glucose (Figure 3a), which was considered as the main substrate for cell growth, was consumed rapidly until about 130 hr (note: both glutamine and pyruvate were depleted before glucose). Shortly before its complete depletion, the cell death increased significantly (Figure 2a). Lactate (Figure 3d) accumulated in the bioreactor until about 130 hr when glucose was depleted. During this phase, glucose was converted mostly to pyruvate producing ATP and other energy precursors. Lactate was produced from pyruvate by a reversible reaction catalyzed by LDH, one of the fastest enzymes of glycolysis that is highly regulated. Here, a noncompetitive inhibition by ATP and pyruvate, previously reported in Brown and Wittenberger (1972) and Coulson and Rabin (1969), with a Michaelis–Menten kinetic was used as this led to a good approximation of the lactate production rate. ATP concentration influences the LDH rate since lactate conversion to pyruvate can regenerate NADH from NAD^+ and, NADH can be converted to ATP. It is likely that for this reason after glucose depletion, cells partially consumed the extracellular lactate. Taking this into account it was possible to capture the increase of ATP concentration observed in the experimental data after glucose and glutamine, and subsequently, pyruvate, were depleted (Figure 3d and further discussion on energy metabolism and product formation in the next section). Lactate consumption by cells has also been observed in other cell lines under different cultivation conditions, and might be controlled by signaling cascades (Genzel et al., 2005; Genzel, Fischer, & Reichl, 2006; Hartley, Walker, Chung, & Morten, 2018; Martínez et al., 2013; Mulukutla et al., 2015; Ryll, Valley, & Wagner, 1994; Schmid & Blanch, 1992; Xie et al., 2015). As an example, for the parental cell line AGE1.HN lactate production has been correlated with PDK4 gene inhibition (Scholz et al., 2011), and in other continuous cell lines its consumption correlated with lactic acidosis (Xie et al., 2015). In this study, two kinetics for LDH were used to account for the switch between lactate production (first 130 hr of cultivation) and consumption (after 130 hr), since intracellular lactate concentration was not considered in the model (Equation 23 in Supporting Information S2, Figure S1b in Supporting Information S4).

Extracellular glutamine and pyruvate (Figures 3c and 3e, respectively) were consumed rapidly and were depleted before glucose at about 100–115 hr. Nevertheless, cell growth continued even after their depletion for a short period of time. Ammonium (Figure 3d) accumulated over the complete cultivation period, with a partial increase of the accumulation rate after glutamine depletion. Finally, glutamate (Figure 3f) accumulated in the media with short periods of uptake on some instances. Interestingly, even after glutamine depletion, glutamate still accumulated. This phenomenon is not uncommon cell cultivations as glutamate is a nonessential amino acid and it is also produced from sources other than glutamine, for example, through lysine and proline catabolism (Lohr et al., 2014; Sonnewald, 2014). Although extracellular amino acids were not quantified in these experiments, batch cultivations with a similar medium composition performed for this cell line demonstrated that most amino acids were not depleted at the end of exponential cell growth phase (Priesnitz et al., 2012). It is thus plausible to assume that even when TCA and glycolysis were shutdown, amino acids catabolism persisted. Another argument for this is the fact that experimental data shows that ammonium, which is released mainly from amino acid catabolism, accumulated until the end of the cultivation (Figure 3d). Assuming that glutamate is mainly produced from amino acid catabolism, it is likely that the glutamate excretion by cells is related to its intracellular excess. This is predicted in our model simulations, where the amino acid degradation rate (Figure S1b in Supporting Information Material S4), which correlates with glutamate production was slightly higher for later cultivation time. This might still be biologically relevant as one of the mechanism that the cells use to keep amino acid homeostasis is the control of amino acid entry or exit through corresponding transporters (Bröer & Bröer, 2017). Overall, for the most important substrates and metabolic by-products, model simulations are well in agreement with experimental data (Figures 3a and 3f). In particular, the segregated cell growth model allowed the estimation of the consumption rates of the substrates glucose, glutamine, and pyruvate (Figures S1a and S1b in Supporting Information Material S4). With these rates as an input for the structured intracellular model of metabolism (below), it was also possible to estimate the release of the metabolic by-products lactate, ammonium, and glutamate (rates used in Figures S1a and S1b in Supporting Information Material S4).

3.3 | Model simulation of intracellular metabolism

In the following, experimental results and model simulations that describe the dynamics of key metabolites of glycolysis, TCA, and energy metabolism for the four cultivations at 0.5–2.5 L scale performed by Rath et al. (Borchers et al., 2013; Rath et al., 2014) are shown. Afterwards, the most relevant intracellular reactions are addressed for two distinct cellular physiological states of AGE1.HN.AAT cells identified over the time course of cultivations for all four batches.

3.4 | Intracellular metabolite concentrations of glycolysis

In the following, model simulations of key metabolites of glycolysis are shown for experimental data over a cultivation period of about 200 hr for all four experiments.

Regarding the upper glycolytic pathway, two interesting dynamics can be observed (Figure 4). The first was a slow accumulation of glucose-6-phosphate (G6P) and fructose-6-phosphate (F6P) until about 96 hr followed by their decrease until depletion. The second was a peak-like accumulation of fructose-1,6-biphosphate (F16P) between 96 and 130 hr. Further aspects

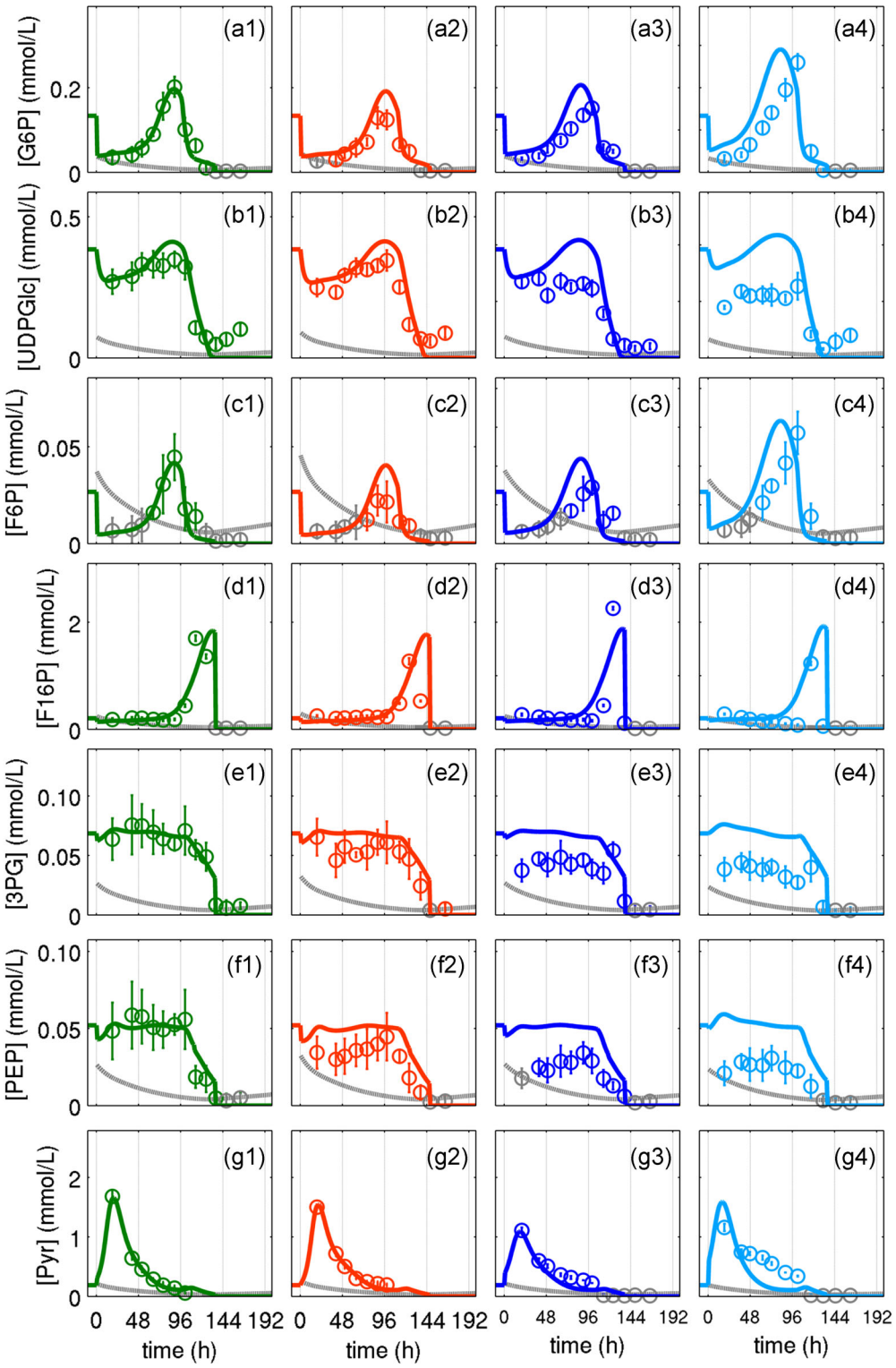

FIGURE 4 Experimental data and model simulations for key metabolites of glycolysis for suspension AGE1.HN.AAT cell growth a chemically defined medium. G6P (A1–4), uracil diphosphate-glucose, UDPGlc (B1–4), F6P (C1–4), fructose-1,6-biphosphate (D1–4), 3-phosphoglutarate (E1–4), phosphoenolpyruvate (F1–4), and intracellular pyruvate (G1–4). Data and error bar represent mean and standard deviation of three technical triplicates for four independent experiments (0.5 L ○, ○ and 2.5 L ○, ○ stirred tank bioreactors); lines: model simulations. Experimental data used for parameter estimation (A1, B1, C1, D1, F1, G1). The gray lines indicate the limit of quantification for each metabolite and the gray data points are under the limit of quantification. F6P, fructose-6-phosphate; G6P, glucose-6-phosphate; UDPGlc, uridine diphosphate glucose [Color figure can be viewed at wileyonlinelibrary.com]

include a high concentration of 3-phosphoglutarate (3GP), uridine diphosphate glucose (UDPGlc) and phosphoenolpyruvate (PEP), which were maintained at relatively high levels until the extracellular glucose was depleted at about 130 hr (Figure 3a). Also, the concentration of intracellular pyruvate decreased over the cultivation time after it achieved its peak concentration at about 20 hr. The fact that most metabolite concentrations remained about constant or even increased until around 96 hr suggests that glucose was not limiting. On the other hand, after glucose was depleted at about 130 hr it coincided with the depletion of all the metabolites of glycolysis.

In all four experiments, experimental data showed similar dynamics for the key metabolites of glycolysis and the model simulations capture these dynamics well. This suggests that useful assumptions regarding the specific kinetics for the glycolytic enzymes were made. Nevertheless, based on the same parameter set, model simulations showed some discrepancies, that is, for PEP and 3PG. This implies that mechanisms used to describe, for instance enolase (ENO) or pyruvate carboxylase (PK) kinetics, might need further improvements. Nevertheless, results also indicate that reasonable assumptions were made for the most critical enzymes in glycolytic control, that is, hexokinase (HK), phosphofructokinase (PFK), and lactate dehydrogenase (LDH) (Tanner et al., 2018). PFK has been described to be closely linked to oscillations frequently found in glycolytic rates (Sola-Penna, Da Silva, Coelho, Marinho-Carvalho, & Zancan, 2010; Yalcin, Telang, Clem, & Chesney, 2009). Furthermore, it is one of the highly controlled enzymes of this pathway with allosteric regulation by energy precursors such as ATP, ADP, and cAMP (Smolen, Baxter, & Byrne, 2014; Sola-Penna et al., 2010; Westermark & Lansner, 2003; Yalcin et al., 2009). For this particular case, a kinetic similar to the Hill kinetic previously applied for other allosteric enzymes was used here (Smolen et al., 2014). With this kinetic for PFK (Equation 15 in Supporting Information Material S2), the glycolytic rates are negatively correlated with the intracellular ATP concentration when glucose was present in the medium (0–130 hr). Another critical enzyme was aldolase (ALD). Without a proper selection of its kinetic (Equation 21 in Supporting Information Material S2), it was not possible to simulate the peak-like behavior of F16P. It was found that the dynamic of F16P is negatively correlated with the specific cell growth rate (Equation 21 in Supporting Information Material S2). Regulation of this enzyme has been previously reported to correlate with changes in cell proliferation, mainly through its localization inside or outside of the nucleus (Mamczur, Gamian, Kolodziej, Dziegiel, & Rakus, 2013).

Taken together, model simulations approximate well the dynamics of most of the glycolytic metabolites. Nevertheless, the unique parameter set used here leads to a better fit of 2.5 L scale when compared to the 0.5 L scale. It is likely that some of the kinetics used, that is, for 3PG and PEP, do not account for minor differences between cultivations performed at both scales. Note that the limit of quantification for each metabolite is influenced by the viable cell volume per milliliter if the volume of sample is constant a higher cell volume per sample decreases the limit of quantification and vice versa).

3.5 | Intracellular metabolites of TCA

Next, model simulations and experimental data regarding metabolites of the TCA cycle for all four batch cultivations of AGE1.HN.AAT cells are presented (Figure 5).

For all key metabolites of the TCA cycle, apart from succinate, the intracellular concentrations were maintained high until around 130 hr when glucose was depleted (Figure 3a). Citrate concentration remained high during cell growth (until around 130 hr) while cis-aconitate concentration was near the limit of quantification. This suggests an equilibrium of aconitate (ACO) in favor of citrate production since isocitrate concentration was around 100-fold lower. The highest concentration of all TCA intermediates was found for succinate exceeding even α-ketoglutarate by a factor of 10. Although α-ketoglutarate is produced from more than one source, contrary to succinate, the concentration of the metabolites can only be related to their related Michaelis–Menten constant. It also clear that α-ketoglutarate dynamics differed at the beginning of the of cultivations even in the same scale. The fact that fumarate concentration remained low and at a level similar to isocitrate suggests that it was rapidly converted to malate by fumarase (FMA), one of fastest enzymes in the TCA cycle.

Apart from succinate at the end of cultivations and α-ketoglutarate at the start of the cultivations, model simulations capture well the dynamics of all metabolites of TCA. This implies that the kinetic mechanisms used were appropriate to describe the metabolic rates involved in production, transport and/or consumption of these metabolites.

In accordance with studies on animal cells (Kim, Tchernyshyov, Semenza, & Dang, 2006; Sable, 2009; Schell et al., 2014; Scholz et al., 2011), analysis of the rates in model simulation showed that the input from glycolysis into the TCA was relatively low. In cancer -derived cell lines, metabolism is typically reprogrammed resulting in a weaker connectivity between glycolysis and TCA through the pyruvate dehydrogenase. For AGE1.HN.AAT cells, this was likely also the case since this enzyme had the lowest maximum activity of all enzymes of the TCA (Rath, 2017). Indeed, model simulations pointed in this direction as the highest metabolic rate input from glycolysis into the TCA in simulations was through pyruvate carboxylase (PC) that converts pyruvate to OAA (Figures S1a and S1b). PC has also been found to significantly contribute to TCA carbon supply according to ^{13}C labeling experiments using Chinese hamster ovary (CHO) cells (Dean & Reddy, 2013). The low activity of PDH and OAA production through PC resulted in a partly reversed TCA to account for the supply of metabolites such as citrate, cis-aconitate and isocitrate (Figure S1a in Supporting Information Material S4). This truncation of TCA has also been

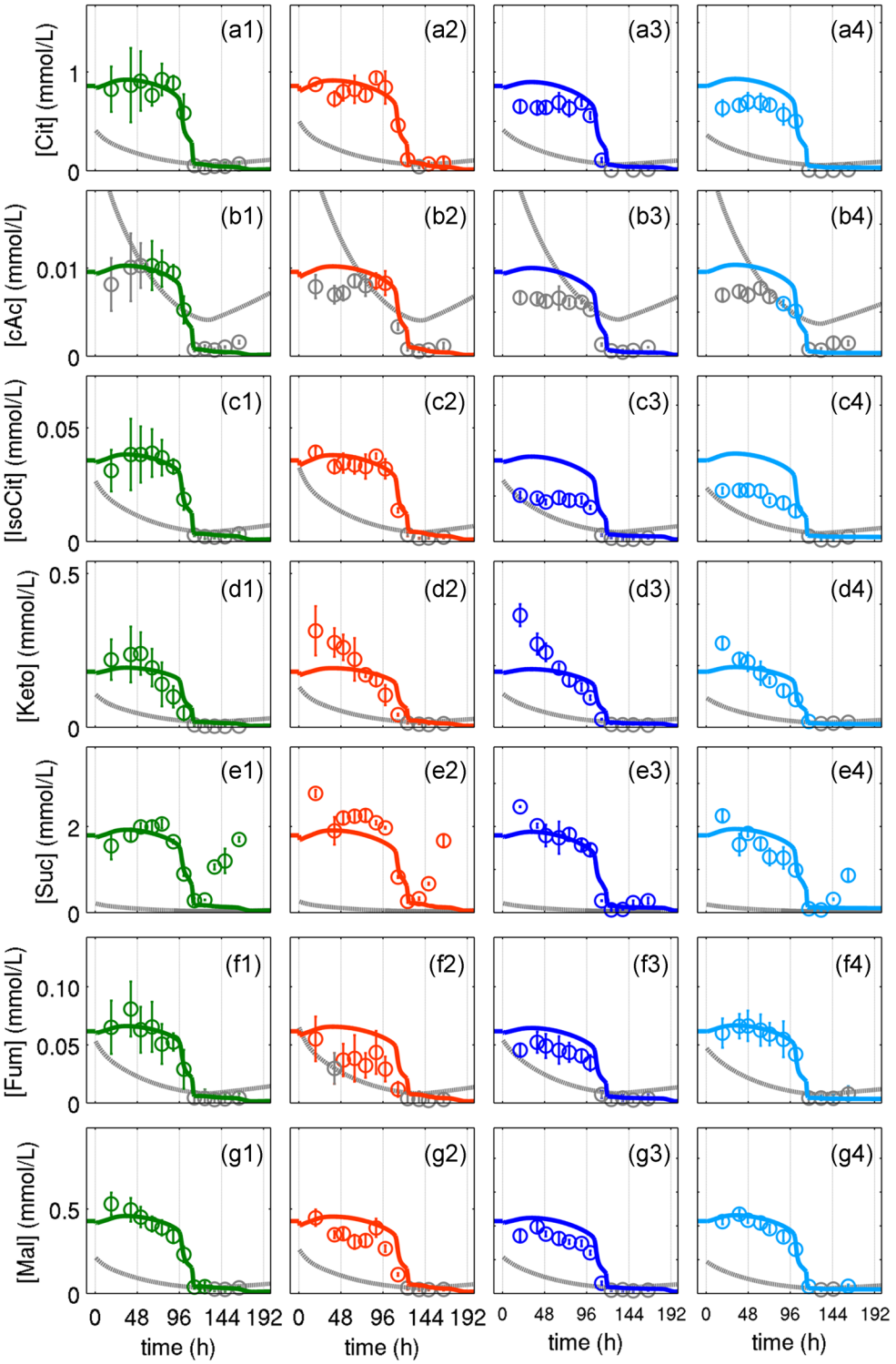

FIGURE 5 Experimental data and model simulations for key metabolites of TCA for suspension AGE1.HN.AAT cell growth a chemically defined medium. Citrate (A1–4), cis-aconitate (B1–4), isocitrate (C1–4), α-ketoglutarate (D1–4), succinate (E1–4), fumarate (F1–4), and malate (G1–4). Data and error bar represent mean and standard deviation of three technical triplicates for four independent experiments (0.5 L ○, ○ and 2.5 L ○, ○ stirred tank bioreactors); lines: model simulations. Experimental data used for parameter estimation (A1, B1, C1, D1, F1, G1). The gray lines indicate the limit of quantification for each metabolite and the gray data points are under the limit of quantification [Color figure can be viewed at wileyonlinelibrary.com]

reported for other cancer cell lines, as it allows generation of citrate and isocitrate, which are important for lipid production (Parlo & Coleman, 1984). For example, in melanoma cells, using ^{13}C labeling it was found that the precursors for lipid production are generated mainly from these reverse reactions in the TCA, and that the main source of these precursors is glutamine (Filipp, Scott, Ronai, Osterman, & Smith, 2012). It is known that glutamine is the main metabolite fueling the TCA since it is converted to α-ketoglutarate, a TCA intermediate (Zheng, 2012). In our modeling approach, α-ketoglutarate production from transamination, where both OAA and glutamate are consumed, was also considered. Previous studies with AGE1.HN cells (Priesnitz et al., 2012) had also elaborated the importance of the transamination reactions. In this model, glutamate is produced from the degradation of amino acids which results in production of ammonium. Furthermore, glutamate can also be produced from α-ketoglutarate through the enzyme glutamate dehydrogenase (GLDH), which consumes ammonium during this process. This reaction plays an important role in the ammonium detoxification (Figure S1b in Supporting Information Material S4). In the model simulations, glutamate was produced through GLDH and amino acid degradation and it was then converted to ketoglutarate by aspartate transaminase with OAA consumption. This is a strong indication that transamination and part of the TCA are used mainly for energy production while the other part of TCA provides intermediates for biosynthesis through citrate (DeBerardinis, Lum, Hatzivassiliou, & Thompson, 2008). However, to better support this theory, the model should be further extended to include lipid synthesis and degradation of other amino acids. This could also potentially benefit the analysis of the relevance of these findings, especially regarding the anaplerotic reaction (PC) addressed previously.

Despite the current limitations, the overall dynamics of the metabolites of the TCA was captured well by simulations, except for succinate at the end of the cultivations and α-ketoglutarate at the start of the cultivations.

3.6 | Energy metabolism and product formation

Next, model simulations and experimental data of intracellular ATP concentration and α1-antitrypsin accumulation in the supernatant are presented for the four batch cultivations (Figure 6).

As long as glucose and glutamine were available in the medium (Figures 3a and 3c), ATP concentrations increased over the cultivation time. Shortly before the depletion of glucose at about 110 hr (Figure 3a), a rapid decrease in ATP concentrations was found for all cultivations. Soon after it increased again (140 hr) and remained high until the end of cultivation. α1-Antitrypsin was produced and exported to the medium while the cells were growing until about 130 hr and remained constant until the end of cultivations. This clearly shows that the production of this protein is growth-related and therefore a simple growth-related kinetic was used to describe its dynamic (Equation 8 in Supporting Information Material S2).

Model simulations capture well the dynamics of ATP and α-1-antrypsin concentration over the time period for all four batch cultivations. This indicates that a simple product formation rate is sufficient to describe its dynamic. For ATP, this indicates that a good balance between consumption (Equation (49) in Supporting Information S2) and production (Equation (45) in Supporting Information S2) was achieved. ATP is produced in both glycolysis (Equation (43) in Supporting Information S2) and oxidative phosphorylation (Equation (44) in Supporting Information S2). According to our model simulations, at least 50% of the total ATP was

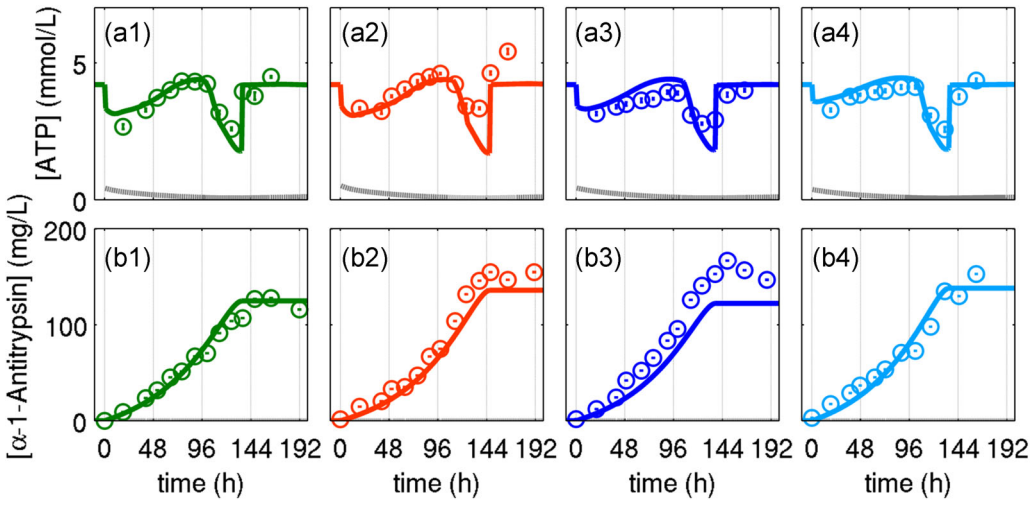

FIGURE 6 Experimental data and model simulations for ATP and α1-antitrypsin for suspension AGE1.HN.AAT cell growth a chemically defined medium. ATP (A1–4) and α1-antitrypsin (B1–4). Data and error bar represent mean and standard deviation of three technical triplicates for four independent experiments (0.5 L ○, ○ and 2.5 L ○, ○ stirred tank bioreactors); lines: model simulations. Experimental data used for parameter estimation (A1, B1). The gray lines indicate the limit of quantification for ATP. ATP, adenosine triphosphate [Color figure can be viewed at wileyonlinelibrary.com]

produced in glycolysis (Figure S1b in Supporting Information Material S4) as long as glucose is present in the medium (until about 130 hr). This agrees well with a previous study which reported a range between 1 and 64% (Zu & Guppy, 2004). In addition, this finding supports the theory that glycolysis could sustain growth demand of AGE1.HN cells as previously suggested in Scholz et al. (2011), that is, that the glycolytic ATP production rate is higher than the simulated ATP consumption for growth (Equation (46) in Supporting Information Material S2 and Figure S1b in Supporting Information Material S4). The model simulation also suggests that the rapid decrease in ATP concentration is mainly due to the depletion of glucose and the subsequent decrease in ATP production in glycolysis (Figure S1b in Supporting Information Material S4). Later, the increase in ATP concentration is due to an increase in oxidation of NADH with lactate consumption (Figure S1b in Supporting Information Material S4). The increase in oxidative phosphorylation also leads to higher estimated theoretical oxygen consumption at the end of the cultivation period (Equation 52 in Supporting Information Material S2 and Figure S1b in Supporting Information Material S4). In this phase, when cells do not grow anymore, ATP is used mainly for maintenance and futile cycles (Equations (47) and (48), respectively in Supporting Information Material S2). Overall, the theoretical oxygen consumption for AGE1.HN.AAT was about 22–106 fmol/cell/h (Figure S1b in Supporting Information Material S4), which is in similar range reported for other continuous cell lines of 7–97 fmol/cell/h (Herst & Berridge, 2007; Sheeran, Streeter, & Dayton, 2013). Interestingly, a much lower oxygen consumption rate was found for the early growth phase (Figure S1b in Supporting Information Material S4) supporting the theory that while there is no limitation of glucose, cells do not use the oxidative phosphorylation pathway at its full potential. A lower oxygen uptake has also been reported previously for murine hybridoma cells for growth without glucose limitation while a higher oxygen uptake was observed near glucose limitation (1–1.5 mM) (Barnabé & Butler, 2000). This confirms again that cells switch to a more efficient metabolism as glucose limitation starts, activating oxidative pathway and lactate consumption.

Overall, model simulations capture very well the dynamics for both ATP and product concentration which indicates that valid biological assumptions were made regarding their kinetics. In particular, theoretical oxygen production rates are well within the range observed for other continuous cell lines.

3.7 | Identification of the most active reactions

Based on the established dynamic model, it was possible to identify two distinct cellular physiological states, which are discussed in the following (Figure 7).

In the first state (Figure 7a), a high glucose consumption rate led to high glycolytic rates. During this phase, most of the glucose was converted to pyruvate, and subsequently to lactate. Glucose entering the cells did not accumulate as its intracellular concentration was always below the limit of detection, that is, glucose was converted rapidly to G6P and, almost as fast, G6P converted to pyruvate. It is well-known that in cancer-derived cell lines glucose is usually converted to lactate (1 Glc: 2 Lac, Warburg effect), even under aerobic conditions (Vander Heiden, Cantley, & Thompson, 2009; Warburg, Wind, & Negelein, 1927). Here, the experimental data show a ratio of 1–1.9 (maximum glucose and lactate concentration in Figure 3a,b). Furthermore, it is reported that 0–40% of G6P generated through HK is channeled to the pentose phosphate pathway by G6PDH (Bonarius et al., 2001; Goudar et al., 2010; Petch & Butler, 1994). For the cultivations considered, the simulated ratio was less than 10% (Figure S1a in Supporting Information Material S4). This ratio

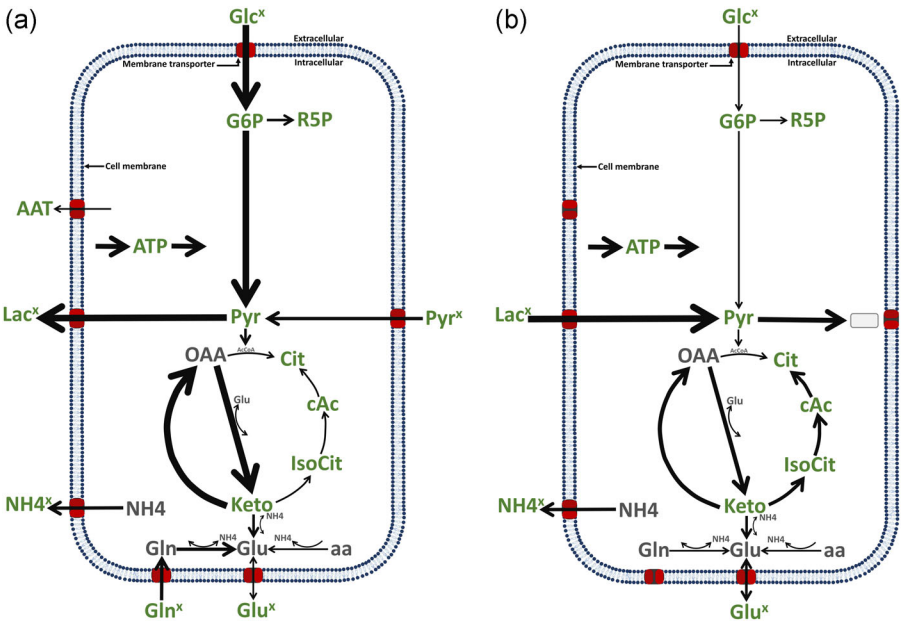

FIGURE 7 The two main cellular physiological states identified for AGE1.HN.AAT cell growth. (a) Cellular physiological state characterized by a high glycolytic rate and a truncated TCA with lactate production and pyruvate uptake. (b) Cellular physiological state characterized by a low glycolytic rate, reactions of the TCA cycle running from α-ketoglutarate to oxaloacetate, amino acid catabolism, ammonium production, and lactate consumption [Color figure can be viewed at wileyonlinelibrary.com]

correlates well with findings from metabolic flux analysis performed by Niklas et al. (2011a), using ^{13}C labeling. Finally, as discussed in the previous section, during this phase (beginning of cultivation until about 130 hr) model simulations suggested that at least 50% of the ATP was produced from glycolysis and a low oxygen consumption rate was simulated.

The second state (Figure 7b) is characterized by the consumption of lactate and the degradation of amino acids to fuel a truncated TCA cycle. This resulted in ammonium secretion even when glutamine was depleted. Since glycolysis also provided OAA for transamination (when the glucose concentration was low), both glycolytic and TCA rates decreased. Accordingly, glutamate consumption in transamination was also lower and glutamate accumulated intracellularly and extracellularly. At this stage, more OAA was produced from citrate degradation by the citrate lyase (CL) indicating that a reverse TCA is required to provide enough OAA to keep transamination active and, therefore, reactions that provide energy precursors. Since transamination shortens the TCA cycle, a more efficient way of producing ATP during limitations can be assumed. Transamination is one option for cells to deal with the weak link of glycolysis to the TCA through PDH to keep ATP production high when needed, in particular, an increase in PDH activity would not help in case glucose is depleted. This hypothesis is supported by the fact that higher PDH activity could lead to OAA depletion because it would lead to citrate production from Acetyl-CoA and OAA, thus shutting down TCA/transamination. Finally, as discussed earlier, during this phase ATP was produced mainly from oxidative phosphorylation and a higher theoretical oxygen consumption rate is observed compared to the first metabolic phase, suggesting that this cellular physiological state is more efficient (Figure S1b in Supporting Information Material S4).

In summary, the main hypothesis derived from these two identified cellular physiological states is that the transamination is a solution to deal with the weak link of glycolysis with TCA through PDH. A compelling argument for this is that according to the model simulations using pyruvate as a substrate, PC produced enough OAA, which was used with glutamate to generate ketoglutarate via transamination. This led ketoglutarate being used as the precursor for the second half of the TCA where energy precursors were produced in substantial amounts.

3.8 | Using the dynamic model for predictions

Finally, the newly established dynamic model was used to perform in silico simulations to address open question regarding the metabolism of AGE1.HN.AAT cells and options to improve process performance. For example, during media optimization (Niklas et al., 2012), it was found that an increase of the pyruvate concentration in the medium

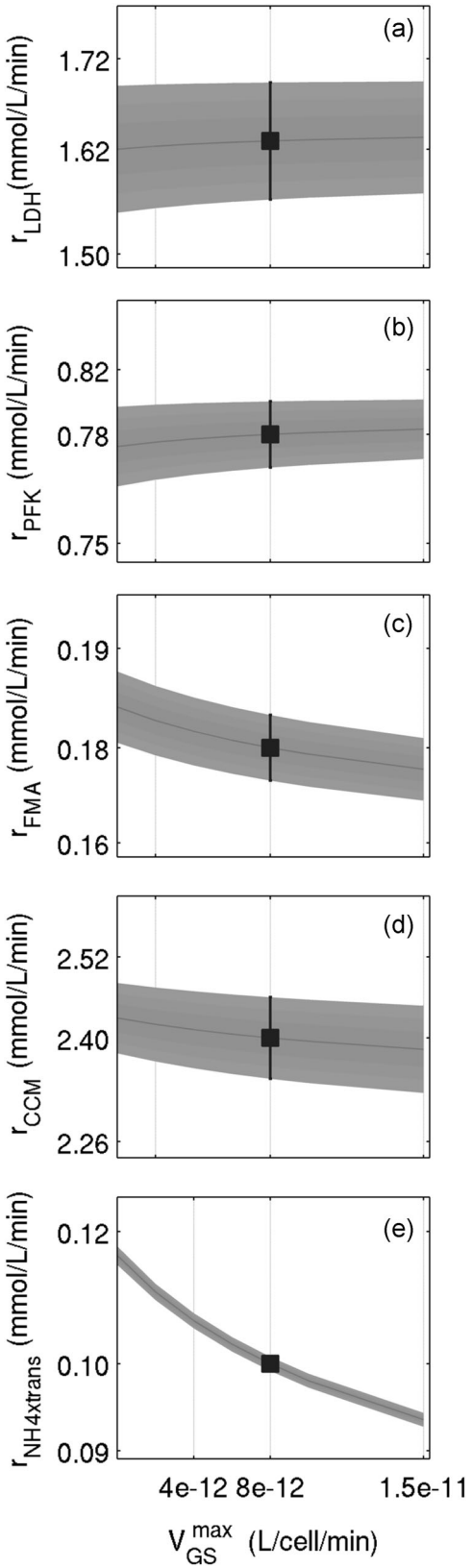

FIGURE 8 Predicted impact of changes in the maximum activity of glutamine synthetase (GS) on selected key reactions of animal cell metabolism. (a) lactate production (r_{LDH}), (b) glycolytic activity (r_{PFK}), (c) TCA activity (r_{FMA}), (d) ATP production (r_{CCM}), and (e) ammonium production ($r_{NH4^x_{trans}}$). The black dots represent the mean rate and standard deviation during the simulation of the four batch experiments. The gray fill: mean and standard deviation of in silico simulations. ATP, adenosine triphosphate

resulted in a negative impact on cell growth and it was then postulated that the increase of pyruvate leads to energy spilling and on the other hand that it did not increase TCA cycle rates. As the intracellular metabolism is highly complex, the established mathematical model can be used to assess possible impacts of such a change in initial conditions on cell intracellular metabolism and provide more concrete insights. Another question relates to the high glutamine synthetase (GS) activity experimentally measured in AGE1.HN cells and whether this could cause ATP dissipation since glutaminase (GLNase) is also expressed in higher levels in these cells (Rath et al., 2014). Regarding the ATP dissipation theory, it is worth mentioning that GS synthetizes glutamine from glutamate, consumes ATP and ammonium, and thus can "dissipate" ATP. Since the GS activity is explicitly considered in the ODEs for glutamine and ATP, simulations for different GS maximum activity levels can be investigated.

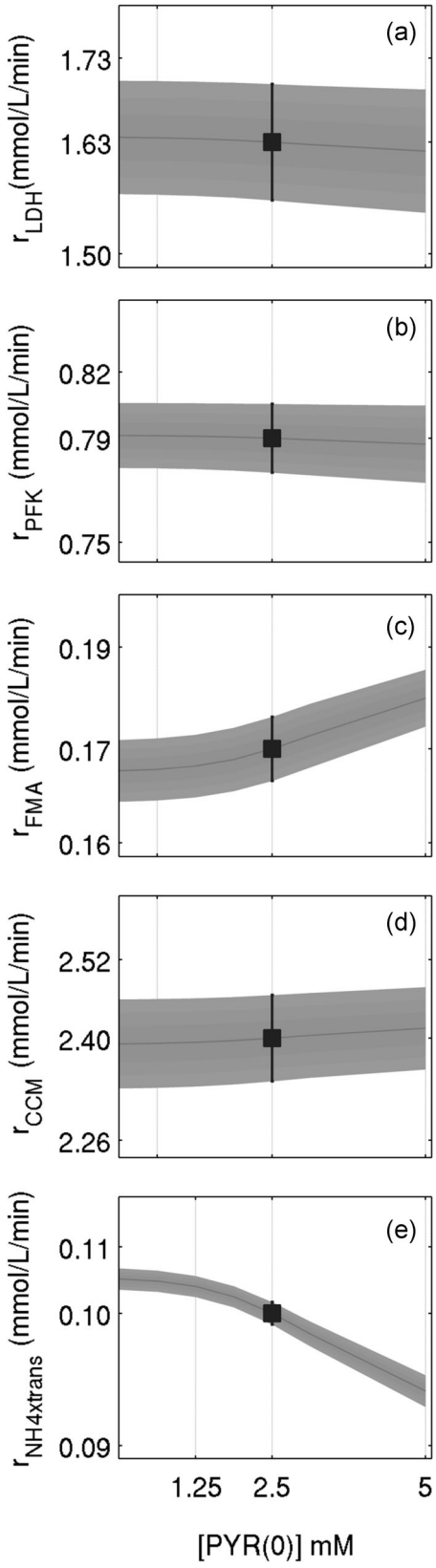

As a starting point, the model was used to evaluate the changes in enzymatic reaction rates to analyze their impact on the dynamics of extracellular substrates and metabolic by-products as well as the cellular physiological state of AGE1.HN.AAT cells during the exponential growth phase. Overall, five key reactions of animal cell metabolism were selected as markers for the intracellular cellular physiological state and analyzed: (a) r_{LDH} (lactate production), (b) r_{PFK} (glycolytic activity), (c) r_{FMA} (TCA activity), (d) r_{CCM} (ATP production), and (e) $r_{NH4^x_{trans}}$ (ammonium production). The results of this study are presented in Figure 8.

In this scenario, changes in the GS activity have almost no impact on both lactate production (Figure 8a) and glycolytic rate (Figure 8b). TCA activity is slightly higher for a lower GS activity (Figure 8c), and the same trend applies to the ATP production rate (Figure 8d). On the other hand, higher GS activity does seem to lead to less ATP net production rate. Finally, the largest impact was on ammonium production as expected, that is, the ammonium production rate is inversely correlated with the GS maximum activity (Figure 8e). Taken together, the results of these in silico simulations suggest changes in GS activity does lead to a minor ATP dissipation. In contrast, the accumulation of ammonium seems to have a stronger effect.

To investigate the changes on intracellular metabolism caused by the changes of the initial concentrations of pyruvate in the media several in silico simulations were performed where the starting concentration of pyruvate was either increased or decreased compared to the experimental data for the four batch used to validate the model and the results are presented in Figure 9.

In this scenario, changes of initial pyruvate concentration in the medium are not expected to have a significant impact on lactate production rate (Figure 9a). Changes in pyruvate concentration also had insignificant impacts on the glycolytic rate (Figure 9b) and the net ATP production rate (Figure 9d). However, changes in the initial

FIGURE 9 Predicted impact of changes in initial extracellular pyruvate concentration ([PYR(0)]) on selected key reactions of animal cell metabolism. (a) lactate production (r_{LDH}), (b) glycolytic activity (r_{PFK}), (c) TCA activity (r_{FMA}), (d) ATP production (r_{CCM}), and (e) ammonium production ($r_{NH4^x_{trans}}$). The black dots represent the mean rate and standard deviation during the simulation of the four batch experiments. The gray fill: mean and standard deviation of in silico simulations. ATP, adenosine triphosphate

pyruvate concentration have an impact on both TCA cycle rate and ammonium production rate (Figures 9c and 9e). In fact, a negative correlation between the initial concentration of pyruvate and the production of ammonium is predicted. This in silico prediction might be biologically relevant as it has been previously reported (Genzel et al., 2005) that high pyruvate concentration in the media resulted in lower ammonium production in different cell lines such as MDCK, CHO-K1, and BHK21. On the other hand, contrary to what was initially postulated (Niklas et al., 2012) for the AGE1.HN.AAT cells, a positive correlation between the initial concentration of pyruvate and TCA cycle rate is predicted. This result is not surprising since this dynamic modeling approach differs from the constraint-based method, which deals with mass balances only. Nevertheless, this finding might also be biologically significant as it has been shown for CHO cells that the addition of pyruvate resulted in an increase in TCA cycle activity (Omasa et al., 2010). Taken together, the results of our in silico analysis point to different hypotheses compared to what was until now assumed regarding the intracellular metabolism of AGE1.HN.AAT cells. They are also supported by findings reported for other cell lines (Genzel et al., 2005; Omasa et al., 2010). Although our model contains over 100 parameters, it is still only a simplified representation of the metabolic network of a human cell line fitted to describe cultivation conditions for a specific training data set. Additional investigations are planned that include various other experimental setups to support further model validation.

4 | CONCLUSIONS

We used a segregated cell growth model coupled to a structured intracellular model of metabolism to describe growth and metabolism of suspension AGE1.HN.AAT cells considered for recombinant human α1-antitrypsin production. The model covers the exponential growth and the death phase. Besides glycolysis, TCA, pentose phosphate pathway, and transamination were considered, and intracellular rates linked to extracellular accumulation of metabolic by-products. The performance of the model was assessed using experimental data (extracellular and intracellular metabolite concentrations, enzyme activities) collected for four batch experiments. Using specific initial conditions and the same set of parameters, the model described extracellular dynamics for growth and death phases well. By taking into account changes in cell volume, dynamics of intracellular concentrations of most metabolites measured and product accumulation could also be fitted well. Based on simulated dynamic rates of key enzymes of the metabolic network, we hypothesize that at least two distinct cellular physiological states exist. The first state is characterized by a high glycolytic rate and a high lactate production rate. This favors high ATP production providing enough energy to sustain cell growth. The second state is characterized by efficient ATP production, a low glycolytic rate, and (partly) reverse TCA cycle reactions. Furthermore, we found that the main link between glycolysis and TCA is through PC, and we discuss the importance of transamination on a truncated TCA. Based on the good fit of model simulation and experimental data, we suggest that control of enzyme activities occurs mainly through substrate or product concentrations.

The developed model was used to perform in silico studies regarding open questions and possible targets for cell line optimization and changes in medium composition. Changes in GS activity seem to have only a minor impact on metabolism and the changes in the initial pyruvate concentration of the medium suggested changes would occur in the metabolism in accordance with previous studies.

Taken together, we show that, with some simplifications and a few basic biological assumptions, it is possible to establish a rather complex dynamic model that not only describes cell growth and product formation in animal cell culture but also links extracellular metabolite dynamics with main intracellular pathways. Furthermore, we showed that such a model could serve as basis to address questions related to cell line engineering, medium design, and as a tool for rational process design.

ACKNOWLEDGMENT

The authors are grateful to Moritz von Stosch and Daniel Rüdiger for their kind revision and suggestions.

CONFLICT OF INTERESTS

The author declares that there are no conflict of interests.

ORCID

João R. C. Ramos http://orcid.org/0000-0002-6832-6774

REFERENCES

Aghamohseni, H., Ohadi, K., Spearman, M., Krahn, N., Moo-Young, M., Scharer, J. M., … Budman, H. M. (2014). Effects of nutrient levels and average culture pH on the glycosylation pattern of camelid-humanized monoclonal antibody. *Journal of Biotechnology*, *186*, 98–109.

Bailey, J. E. (1998). Mathematical modeling and analysis in biochemical engineering: Past accomplishments and future opportunities. *Biotechnology Progress*, *14*(1), 8–20.

Barford, J., Phillips, P., & Harbour, C. (1992). Simulation of animal cell metabolism. *Mathematics and Computers in Simulation*, *33*(5–6), 397–402.

Barnabé, N., & Butler, M. (2000). The effect of glucose and glutamine on the intracellular nucleotide pool and oxygen uptake rate of a murine hybridoma. *Cytotechnology*, *34*(1–2), 47–57.

Batt, B. C., & Kompala, D. S. (1989). A structured kinetic modeling framework for the dynamics of hybridoma growth and monoclonal antibody production in continuous suspension cultures. *Biotechnology and Bioengineering*, *34*(4), 515–531.

Bazil, J. N., Buzzard, G. T., & Rundell, A. E. (2010). Modeling mitochondrial bioenergetics with integrated volume dynamics. *PLoS Computational Biology*, *6*(1), e1000632.

Blanchard, V., Liu, X., Eigel, S., Kaup, M., Rieck, S., Janciauskiene, S., … Berger, M. (2011). N-glycosylation and biological activity of recombinant human alpha1-antitrypsin expressed in a novel human neuronal cell line. *Biotechnology and Bioengineering*, *108*(9), 2118–2128.

Blondeel, E. J. M., & Aucoin, M. G. (2018). Supplementing glycosylation: A review of applying nucleotide-sugar precursors to growth medium to affect therapeutic recombinant protein glycoform distributions. *Biotechnology Advances*, *36*(5), 1505–1523.

Bonarius, H. P. J., Özemre, A., Timmerarends, B., Skrabal, P., Tramper, J., Schmid, G., & Heinzle, E. (2001). Metabolic-flux analysis of continuously cultured hybridoma cells using 13CO2 mass spectrometry in combination with 13C-lactate nuclear magnetic resonance spectroscopy and metabolite balancing. *Biotechnology and Bioengineering*, *74*(6), 528–538.

Borchers, S., Freund, S., Rath, A., Streif, S., Reichl, U., & Findeisen, R. (2013). Identification of growth phases and influencing factors in cultivations with AGE1.HN cells using set-based methods. *PLoS One*, *8*(8), e68124.

Brendel, M., & Marquardt, W. (2008). Experimental design for the identification of hybrid reaction models from transient data. *Chemical Engineering Journal*, *141*(1–3), 264–277.

Brown, A. T., & Wittenberger, C. L. (1972). Fructose-1,6-diphosphate-dependent lactate dehydrogenase from a cariogenic streptococcus: Purification and regulatory properties. *Journal of Bacteriology*, *110*(2), 604–615.

Bröer, S., & Bröer, A. (2017). Amino acid homeostasis and signalling in mammalian cells and organisms. *Biochemical Journal*, *474*(12), 1935–1963.

Chassagnole, C., Noisommit-Rizzi, N., Schmid, J. W., Mauch, K., & Reuss, M. (2002). Dynamic modeling of the central carbon metabolism of *Escherichia coli*. *Biotechnology and Bioengineering*, *79*(1), 53–73.

Cohen, S. D., & Hindmarsh, A. C. (1996). CVODE, a stiff/nonstiff ODE solver in C. *Computers in Physics*, *10*(2), 138–143.

Coulson, C. J., & Rabin, B. R. (1969). Inhibition of lactate dehydrogenase by high concentrations of pyruvate: The nature and removal of the inhibitor. *FEBS Letters*, *3*(5), 333–337.

Dean, J., & Reddy, P. (2013). Metabolic analysis of antibody producing CHO cells in fed-batch production. *Biotechnology and Bioengineering*, *110*(6), 1735–1747.

DeBerardinis, R. J., Lum, J. J., Hatzivassiliou, G., & Thompson, C. B. (2008). The biology of cancer: Metabolic reprogramming fuels cell growth and proliferation. *Cell Metabolism*, *7*(1), 11–20.

Egea, J. A., Balsa-Canto, E., García, M. S. G., & Banga, J. R. (2009). Dynamic optimization of nonlinear processes with an enhanced scatter search method. *Industrial and Engineering Chemistry Research*, *48*(9), 4388–4401.

Egea, J. A., Martí, R., & Banga, J. R. (2010). An evolutionary method for complex-process optimization. *Computers and Operations Research*, *37*(2), 315–324.

Filipp, F. V., Scott, D. A., Ronai, Z. A., Osterman, A. L., & Smith, J. W. (2012). Reverse TCA cycle flux through isocitrate dehydrogenases 1 and 2 is required for lipogenesis in hypoxic melanoma cells. *Pigment Cell & Melanoma Research*, *25*(3), 375–383.

Galleguillos, S. N., Ruckerbauer, D., Gerstl, M. P., Borth, N., Hanscho, M., & Zanghellini, J. (2017). What can mathematical modelling say about CHO metabolism and protein glycosylation? *Computational and Structural Biotechnology Journal*, *15*, 212–221.

Genzel, Y., Fischer, M., & Reichl, U. (2006). Serum-free influenza virus production avoiding washing steps and medium exchange in large-scale microcarrier culture. *Vaccine*, *24*(16), 3261–3272.

Genzel, Y., Ritter, J. B., König, S., Alt, R., & Reichl, U. (2005). Substitution of glutamine by pyruvate to reduce ammonium formation and growth inhibition of mammalian cells. *Biotechnology Progress*, *21*(1), 58–69.

Gombert, A. K., & Nielsen, J. (2000). Mathematical modelling of metabolism. *Current Opinion in Biotechnology*, *11*(2), 180–186.

Goudar, C., Biener, R., Boisart, C., Heidemann, R., Piret, J., de Graaf, A., & Konstantinov, K. (2010). Metabolic flux analysis of CHO cells in perfusion culture by metabolite balancing and 2D [13C, 1H] COSY NMR spectroscopy. *Metabolic Engineering*, *12*(2), 138–149.

Hartley, F., Walker, T., Chung, V., & Morten, K. (2018). Mechanisms driving the lactate switch in Chinese hamster ovary cells. *Biotechnology and Bioengineering*, *115*(8), 1890–1903.

Vander Heiden, M. G., Cantley, L. C., & Thompson, C. B. (2009). Understanding the Warburg effect: The metabolic requirements of cell proliferation. *Science*, *324*(5930), 1029–1033.

Herst, P. M., & Berridge, M. V. (2007). Cell surface oxygen consumption: A major contributor to cellular oxygen consumption in glycolytic cancer cell lines. *Biochimica et Biophysica Acta – Bioenergetics*, *1767*(2), 170–177.

Hwang, D., Stephanopoulos, G., & Chan, C. (2004). Inverse modeling using multi-block PLS to determine the environmental conditions that provide optimal cellular function. *Bioinformatics*, *20*(4), 487–499.

Hyde, R., Taylor, P. M., & Hundal, H. S. (2003). Amino acid transporters: Roles in amino acid sensing and signalling in animal cells. *Biochemical Journal*, *373*(1), 1–18.

Janke, R. (2012). Investigation of mammalian cell metabolism by quantification of key metabolic enzyme activities (Doctoral dissertation, Otto von Guericke University Magdeburg). Retrieved from http://hdl.handle.net/11858/00-001M-0000-0013-883A-5

Salway, J. G. (2004). Summary for Policymakers. *Climate Change 2013 - The Physical Science Basis*, *16(1A)*, 1–30.

Jimenez del Val, I., Nagy, J. M., & Kontoravdi, C. (2011). A dynamic mathematical model for monoclonal antibody N-linked glycosylation and nucleotide sugar donor transport within a maturing Golgi apparatus. *Biotechnology Progress*, *27*(6), 1730–1743.

Khodayari, A., Zomorrodi, A. R., Liao, J. C., & Maranas, C. D. (2014). A kinetic model of *Escherichia coli* core metabolism satisfying multiple sets of mutant flux data. *Metabolic Engineering*, *25*, 50–62.

Kim, J. W., Tchernyshyov, I., Semenza, G. L., & Dang, C. V. (2006). HIF-1-mediated expression of pyruvate dehydrogenase kinase: A metabolic switch required for cellular adaptation to hypoxia. *Cell Metabolism*, *3*(3), 177–185.

Kreutz, C., & Timmer, J. (2009). Systems biology: Experimental design. *FEBS Journal*, *276*(4), 923–942.

Kyriakopoulos, S., Ang, K. S., Lakshmanan, M., Huang, Z., Yoon, S., Gunawan, R., & Lee, D. Y. (2018). Kinetic modeling of mammalian cell culture bioprocessing: The quest to advance biomanufacturing. *Biotechnology Journal*, *13*(3), 1700229.

König, M., Bulik, S., & Holzhütter, H. G. (2012). Quantifying the contribution of the liver to glucose homeostasis: A detailed kinetic model of human hepatic glucose metabolism. *PLoS Computational Biology*, *8*(6), e1002577.

Lee, J. M., Gianchandani, E. P., & Papin, J. A. (2006). Flux balance analysis in the era of metabolomics. *Briefings in Bioinformatics*, *7*(2), 140–150.

Lee, S. Y., Park, J. M., & Kim, T. Y. (2011). Application of metabolic flux analysis in metabolic engineering, *Methods in Enzymology* (498, 1st ed.). Elsevier Inc.

Li, F., Vijayasankaran, N., Shen, A. Y., Kiss, R., & Amanullah, A. (2010). Cell culture processes for monoclonal antibody production. *mAbs*, *2*(5), 466–479.

Lohr, V., Hädicke, O., Genzel, Y., Jordan, I., Büntemeyer, H., Klamt, S., & Reichl, U. (2014). The avian cell line AGE1.CR.pIX characterized by metabolic flux analysis. *BMC Biotechnology*, *14*, 72.

Luni, C., Marth, J. D., & Doyle, F. J. (2012). Computational modeling of glucose transport in pancreatic β-cells identifies metabolic thresholds and therapeutic targets in diabetes. *PLoS One*, *7*(12), 1–8.

Mamczur, P., Gamian, A., Kolodziej, J., Dziegiel, P., & Rakus, D. (2013). Nuclear localization of aldolase A correlates with cell proliferation. *Biochimica et Biophysica Acta (BBA) - Molecular Cell Research*, *1833*(12), 2812–2822.

Mandenius, C.-F., & Brundin, A. (2008). Review: Biocatalysts and bioreactor design. *Biotechnology Progress*, *24*, 1191–1203.

Martínez, V. S., Dietmair, S., Quek, L. -E., Hodson, M. P., Gray, P., & Nielsen, L. K. (2013). Flux balance analysis of CHO cells before and after a metabolic switch from lactate production to consumption. *Biotechnology and Bioengineering*, *110*(2), 660–666.

Marín-Hernández, A., Gallardo-Pérez, J. C., Rodríguez-Enríquez, S., Encalada, R., Moreno-Sánchez, R., & Saavedra, E. (2011). Modeling cancer glycolysis. *Biochimica et Biophysica Acta - Bioenergetics*, *1807*(6), 755–767.

Müller, A., & Bockmayr, A. (2012). Thermodynamic Constraints for Metabolic Networks (Master Thesis, Free University of Berlin). Retrieved from https://refubium.fu-berlin.de/bitstream/handle/fub188/11116/diss_reimers_gedreht.pdf

Mulukutla, B. C., Yongky, A., Grimm, S., Daoutidis, P., & Hu, W. S. (2015). Multiplicity of steady states in glycolysis and shift of metabolic state in cultured mammalian cells. *PLoS One*, *10*(3), 1–20.

Nazaret, C., Heiske, M., Thurley, K., & Mazat, J. P. (2009). Mitochondrial energetic metabolism: A simplified model of TCA cycle with ATP production. *Journal of Theoretical Biology*, *258*(3), 455–464.

Nielsen, L. K., Reid, S., & Greenfield, P. F. (1997). Cell cycle model to describe animal cell size variation and lag between cell number and biomass dynamics. *Biotechnology and Bioengineering*, *56*, 372–379.

Niklas, J., Priesnitz, C., Rose, T., Sandig, V., & Heinzle, E. (2012). Primary metabolism in the new human cell line AGE1.HN at various substrate levels: Increased metabolic efficiency and α 1 -antitrypsin production at reduced pyruvate load. *Applied Microbiology and Biotechnology*, *93*(4), 1637–1650.

Niklas, J., Sandig, V., & Heinzle, E. (2011a). Metabolite channeling and compartmentation in the human cell line AGE1.HN determined by 13C labeling experiments and 13C metabolic flux analysis. *Journal of Bioscience and Bioengineering*, *112*(6), 616–623.

Niklas, J., Schräder, E., Sandig, V., Noll, T., & Heinzle, E. (2011b). Quantitative characterization of metabolism and metabolic shifts during growth of the new human cell line AGE1.HN using time resolved metabolic flux analysis. *Bioprocess and Biosystems Engineering*, *34*(5), 533–545.

Noguchi, R., Kubota, H., Yugi, K., Toyoshima, Y., Komori, Y., Soga, T., & Kuroda, S. (2013). The selective control of glycolysis, gluconeogenesis and glycogenesis by temporal insulin patterns. *Molecular Systems Biology*, *9*(664), 664.

Omasa, T., Furuichi, K., Iemura, T., Katakura, Y., Kishimoto, M., & Suga, K. I. (2010). Enhanced antibody production following intermediate addition based on flux analysis in mammalian cell continuous culture. *Bioprocess and Biosystems Engineering*, *33*(1), 117–125.

Orth, J. D., Thiele, I., & Palsson, B. Ø. (2010). What is flux balance analysis? *Nature Biotechnology*, *28*(3), 245–248.

Ozturk, S. S., & Palsson, B. O. (1990). Chemical decomposition of glutamine in cell culture media: Effect of media type, pH, and serum concentration. *Biotechnology Progress*, *6*(2), 121–128.

Parks, R. J. (2005). Adenovirus protein IX: A new look at an old protein. *Molecular Therapy*, *11*(1), 19–25.

Parlo, R. A., & Coleman, P. S. (1984). Enhanced rate of citrate export from cholesterol-rich hepatoma mitochondria. The truncated Krebs cycle and other metabolic ramifications of mitochondrial membrane cholesterol. *Journal of Biological Chemistry*, *259*(16), 9997–10003.

Petch, D., & Butler, M. (1994). Profile of energy metabolism in a murine hybridoma: Glucose and glutamine utilization. *Journal of Cellular Physiology*, *161*(1), 71–76.

Priesnitz, C., Niklas, J., Rose, T., Sandig, V., & Heinzle, E. (2012). Metabolic flux rearrangement in the amino acid metabolism reduces ammonium stress in the α1-antitrypsin producing human AGE1.HN cell line. *Metabolic Engineering*, *14*(2), 128–137.

Rath, A. (2017). Characterization of cell growth, metabolism and recombinant protein production during transient and steady state conditions for the human cell line AGE1.HN-AAT (Doctoral dissertation, Otto von Guericke University Magdeburg). Retrieved from https://pure.mpg.de/pubman/item/item_2508673_4

Rath, A. G., Rehberg, M., Janke, R., Genzel, Y., Scholz, S., Noll, T., … Reichl, U. (2014). The influence of cell growth and enzyme activity changes on intracellular metabolite dynamics in AGE1.HN.AAT cells. *Journal of Biotechnology*, *178*(1), 43–53.

Rehberg, M., Rath, A., Ritter, J. B., Genzel, Y., & Reichl, U. (2014a). Changes in intracellular metabolite pools during growth of adherent MDCK cells in two different media. *Applied Microbiology and Biotechnology*, *98*(1), 385–397.

Rehberg, M., Ritter, J. B., & Reichl, U. (2014b). Glycolysis is governed by growth regime and simple enzyme regulation in adherent MDCK cells. *PLoS Computational Biology*, *10*(10), e1003885.

Rehberg, M., Ritter, J. B., Genzel, Y., Flockerzi, D., & Reichl, U. (2013a). The relation between growth phases, cell volume changes and metabolism of adherent cells during cultivation. *Journal of Biotechnology*, *164*(4), 489–499.

Rehberg, M., Wetzel, M., Ritter, J. B., & Reichl, U. (2013b). The regulation of glutaminolysis and citric acid cycle activity during mammalian cell cultivation. *12th IFAC Symposium on Computer Applications in Biotechnology*, *12*, 48–53.

Ritter, J. B., Wahl, A. S., Freund, S., Genzel, Y., & Reichl, U. (2010). Metabolic effects of influenza virus infection in cultured animal cells: Intra- and extracellular metabolite profiling. *BMC Systems Biology*, *4*(1), 61.

Rizzi, M., Baltes, M., Theobald, U., & Reuss, M. (1997). In vivo analysis of metabolic dynamics in *Saccharomyces cerevisiae*: II. Mathematical model. *Biotechnology and Bioengineering*, *55*(4), 592–608.

Ryll, T., Valley, U., & Wagner, R. (1994). Biochemistry of growth inhibition by ammonium ions in mammalian cells. *Biotechnology and Bioengineering*, *44*(2), 184–193.

Sable, H. Z. (2009). Biochemistry: The molecular basis of cell structure and function (Lehninger, Albert L.). *Journal of Chemical Education*, *48*(4), A288.

Sanderson, C., Barford, J., & Barton, G. (1999). A structured, dynamic model for animal cell culture systems. *Biochemical Engineering Journal*, *3*(3), 203–211.

Schell, J. C., Olson, K. A., Jiang, L., Hawkins, A. J., VanVranken, J. G., Xie, J., & Rutter, J. (2014). A role for the mitochondrial pyruvate carrier as a repressor of the warburg effect and colon cancer cell growth. *Molecular Cell*, *56*(3), 400–413.

Schmid, G., & Blanch, H. W. (1992). Extra- and intracellular metabolite concentrations for murine hybridoma cells. *Applied Microbiology and Biotechnology*, *36*(5), 621–625.

Schmidt, H., & Jirstrand, M. (2006). Systems Biology Toolbox for MATLAB: A computational platform for research in systems biology. *Bioinformatics*, *22*(4), 514–515.

Scholz, S., Luebbecke, M., Rath, A., Schraeder, E., Rose, T., Büntemeyer, H., … Noll, T. (2011). Characterization of the human AGE1.HN cell line: A systems biology approach. *BMC Proceedings*, *5*(Suppl 8), P78.

Sheeran, P., Streeter, J., & Dayton, P. (2013). Towards ultrasound molecular imaging with phase-change contrast agents. *Ultrasound Medical Biology*, *39*, 893–902.

Sidoli, F. R., Mantalaris, A., & Asprey, S. P. (2004). Modelling of mammalian cells and cell culture processes. *Cytotechnology*, *44*(1–2), 27–46.

Smolen, P. D., Baxter, D. A., & Byrne, J. H. (2014). Modeling and Analysis of Intracellular Signaling Pathways, *From Molecules to Networks: An Introduction to Cellular and Molecular Neuroscience* (3rd ed, pp. 175–205). California: Academic Press.

Sola-Penna, M., Da Silva, D., Coelho, W. S., Marinho-Carvalho, M. M., & Zancan, P. (2010). Regulation of mammalian muscle type 6-phosphofructo-1-kinase and its implication for the control of the metabolism. *IUBMB Life*, *62*(11), 791–796.

Sonnewald, U. (2014). Glutamate synthesis has to be matched by its degradation – Where do all the carbons go? *Journal of Neurochemistry*, *131*(4), 399–406.

Stephanopoulos, G. (1999). Metabolic fluxes and metabolic engineering. *Metabolic Engineering*, *1*(1), 1–11.

Stephanopoulos, G., & Sinskey, A. J. (1993). Metabolic engineering – Methodologies and future prospects. *Trends in Biotechnology*, *11*(9), 392–396.

Stephanopoulos, G., & Stafford, D. E. (2002). Metabolic engineering: A new frontier of chemical reaction engineering. *Chemical Engineering Science*, *57*(14), 2595–2602.

von Stosch, M., & Willis, M. J. (2017). Intensified design of experiments for upstream bioreactors. *Engineering in Life Sciences*, *17*(11), 1173–1184.

Tanner, L. B., Goglia, A. G., Wei, M. H., Sehgal, T., Parsons, L. R., Park, J. O., … Rabinowitz, J. D. (2018). Four key steps control glycolytic flux in mammalian cells. *Cell Systems*, *7*(1), 49–62.e8.

de Tremblay, M., Perrier, M., Chavarie, C., & Archambault, J. (1992). Optimization of fed-batch culture of hybridoma cells using dynamic programming: Single and multi feed cases. *Bioprocess Engineering*, *7*(5), 229–234.

Uldry, M., Ibberson, M., Hosokawa, M., & Thorens, B. (2002). GLUT2 is a high affinity glucosamine transporter. *FEBS Letters*, *524*(1–3), 199–203.

Vicente, T., Mota, J. P. B., Peixoto, C., Alves, P. M., & Carrondo, M. J. T. (2011). Rational design and optimization of downstream processes of virus particles for biopharmaceutical applications: Current advances. *Biotechnology Advances*, *29*(6), 869–878.

Warburg, O., Wind, F., & Negelein, E. (1927). I. Killing-off of tumor cells in vitro. *The Journal of General Physiology*, *8*(6), 519–530.

Westermark, P. O., & Lansner, A. (2003). A model of phosphofructokinase and glycolytic oscillations in the pancreatic beta-cell. *Biophysical Journal*, *85*(July), 126–139.

Xie, J., Wu, H., Dai, C., Pan, Q., Ding, Z., Hu, D., … Hu, X. (2015). Beyond Warburg effect – Dual metabolic nature of cancer cells. *Scientific Reports*, *4*(1), 4927.

Xie, L., & Wang, D. I. C. (1996). Energy metabolism and ATP balance in animal cell cultivation using a stoichiometrically based reaction network. *Biotechnology and Bioengineering*, *52*(5), 591–601.

Yalcin, A., Telang, S., Clem, B., & Chesney, J. (2009). Regulation of glucose metabolism by 6-phosphofructo-2-kinase/fructose-2,6-bisphosphatases in cancer. *Experimental and Molecular Pathology*, *86*(3), 174–179.

Zheng, J. (2012). Energy metabolism of cancer: Glycolysis versus oxidative phosphorylation (review). *Oncology Letters*, *4*(6), 1151–1157.

Zhou, F., Bi, J. X., Zeng, A. P., & Yuan, J. Q. (2006). A macrokinetic and regulator model for myeloma cell culture based on metabolic balance of pathways. *Process Biochemistry*, *41*(10), 2207–2217.

Zu, X. L., & Guppy, M. (2004). Cancer metabolism: Facts, fantasy, and fiction. *Biochemical and Biophysical Research Communications*, *313*(3), 459–465.

SUPPORTING INFORMATION

Additional supporting information may be found online in the Supporting Information section.

How to cite this article: Ramos JRC, Rath AG, Genzel Y, Sandig V, Reichl U. A dynamic model linking cell growth to intracellular metabolism and extracellular by-product accumulation. *Biotechnology and Bioengineering*. 2020;117: 1533–1553. https://doi.org/10.1002/bit.27288